

Enrichment of the Galactic disc with neutron-capture elements: Mo and Ru

T. Mishenina¹ *, M. Pignatari^{2,3,6} † *, T. Gorbaneva¹, C. Travaglio^{4,5} † ,
 B. Côté^{3,6} † , F.-K. Thielemann^{7,8}, C. Soubiran⁹

¹ *Astronomical Observatory, Odessa National University, Shevchenko Park, 65014, Odessa, Ukraine*

² *E.A. Milne Centre for Astrophysics, Dept of Physics & Mathematics, University of Hull, HU6 7RX, United Kingdom*

³ *Konkoly Observatory, Hungarian Academy of Sciences, Konkoly Thege Miklos ut 15-17, H-1121 Budapest, Hungary*

⁴ *INFN, University of Turin, Via Pietro Giuria 1, 10025 Turin, Italy*

⁵ *B2FH Association, Turin, Italy*

⁶ *Joint Institute for Nuclear Astrophysics - Center for the Evolution of the Elements, USA*

⁷ *Department of Physics, University of Basel, Klingelbergstrasse 82, 4056 Basel, Switzerland*

⁸ *GSI Helmholtzzentrum fr Schwerionenforschung, Planckstrasse 1, D-64291 Darmstadt, Germany*

⁹ *Laboratoire d’Astrophysique de Bordeaux, Univ. Bordeaux - CNRS, B18N, allée Geoffroy Saint-Hilaire, 33615 Pessac, France*

Accepted 2015 xxx. Received 2015 xxx; in original form 2015 xxx

ABSTRACT

We present new observational data for the heavy elements molybdenum (Mo, $Z = 42$) and ruthenium (Ru, $Z = 44$) in F-, G-, and K-stars belonging to different substructures of the Milky Way. The range of metallicity covered is $-1.0 < [\text{Fe}/\text{H}] < +0.3$. The spectra of Galactic disc stars have a high resolution of 42,000 and 75,000 and signal-to-noise ratio better than 100. Mo and Ru abundances were derived by comparing the observed and synthetic spectra in the region of Mo I lines at 5506, 5533 Å for 209 stars and Ru I lines at 4080, 4584, 4757 Å for 162 stars using the LTE approach. For all the stars, the Mo and Ru abundance determinations are obtained for the first time with an average error of 0.14 dex. This is the first extended sample of stellar observations for Mo and Ru in the Milky Way disc, and together with earlier observations in halo stars it is pivotal in providing a complete picture of the evolution of Mo and Ru across cosmic timescales.

The Mo and Ru abundances were compared with those of the neutron-capture elements (Sr, Y, Zr, Ba, Sm, Eu). The complex nucleosynthesis history of Mo and Ru is compared with different Galactic Chemical Evolution (GCE) simulations. In general, present theoretical GCE simulations show underproduction of Mo and Ru at all metallicities compared to observations. This highlights a significant contribution of nucleosynthesis processes not yet considered in our simulations. A number of possible scenarios are discussed.

Key words: stars: abundances – stars: late-type – Galaxy: disc – Galaxy: evolution

1 INTRODUCTION

The elements molybdenum (Mo, $Z = 42$) and ruthenium (Ru, $Z = 44$) are located just above the first neutron-shell closure beyond iron, at $N=50$. They both have seven stable isotopes, providing an ideal benchmark for nuclear astrophysics. The isotopes ^{92–94}Mo and ^{94–96}Ru are classically defined as p -only nuclei, i.e. they can be made by the γ process or by some p -process component, but not by neutron-

capture processes. Their high concentration in the solar system compared to other neutron-rich Mo and Ru isotopes is still a major puzzle to be solved (e.g. Arnould & Goriely 2003; Rauscher et al. 2013; Pignatari et al. 2016a, and references therein). ⁹⁶Mo and ¹⁰⁰Ru are classified as s -only isotopes, i.e. they can be made by the slow neutron-capture process or s -process (e.g. Käppeler et al. 2011, and references therein). ¹⁰⁰Mo and ¹⁰⁴Ru are not efficiently produced via the s -process (e.g. Bisterzo et al. 2014). They are classified as r -only isotopes, i.e. they are made mostly by some of the rapid neutron-capture process components, or r -process (Cowan et al. 2019, and references therein). Fi-

* tmishenina@ukr.net; * mpignatari@gmail.com

† The NuGrid collaboration, http://www.nugridstars.org

nally, the intermediate neutron-capture process (*i*-process; Cowan & Rose 1977) have been shown to produce efficiently the Mo stable isotopes ^{95}Mo and ^{97}Mo , and preliminary evaluations of the *i*-process contribution to Mo and Ru have been reported in (Côté et al. 2018a). Therefore, studying these elements in the context of Galactic Chemical Evolution (GCE) can provide valuable diagnostics on the nucleosynthesis processes described above.

The *s*-process component of Mo and Ru is made by the main *s*-process component between Sr and Pb, that is produced by Asymptotic Giant Branch stars (AGB stars, e.g. Gallino et al. 1998; Busso, Gallino & Wasserburg 1999). In these stars most of the neutrons are released by the $^{13}\text{C}(\alpha, n)^{16}\text{O}$ reaction in the radiative ^{13}C -pocket, formed right after the third dredge-up event (e.g. Straniero et al. 1995). The rest of the neutrons are supplied by the partial activation of the $^{22}\text{Ne}(\alpha, n)^{25}\text{Mg}$ reaction during the convective thermal pulse (Busso, Gallino & Wasserburg 1999; Herwig 2005; Karakas & Lattanzio 2014, and reference therein). The weak *s*-process component in the solar system originates in massive stars, and is mostly due to the $^{22}\text{Ne}(\alpha, n)^{25}\text{Mg}$ activation in the convective He-burning core and in the convective C-burning shell (e.g. The, El Eid & Meyer 2007; Pignatari et al. 2010, and references therein). The weak *s*-process contributes to no more than few per cent to the solar abundance of Mo and Ru (Travaglio et al. 2004). The relevance of additional *s*-process production in rotating massive stars to GCE is still being debated, in the early Galaxy as well as for the solar system (e.g. Pignatari et al. 2008; Maeder, Meynet & Chiappini 2015; Cescutti et al. 2015; Frischknecht et al. 2016; Choplin et al. 2018).

The origin of the *r*-process abundances beyond Fe is still matter of debate. Several astrophysical scenarios have been proposed: 1) neutrino-driven winds from core-collapse supernovae (CCSNe) (e.g. Hoffman et al. 1994; Hoffman, Woosley & Qian 1997; Wanajo et al. 2001; Farouqi et al. 2009; Arcones & Montes 2011; Kratz, Farouqi & Möller 2014) or electron-capture supernovae (ECSNe), i.e. collapsing O-Mg-Ne cores (Wanajo, Janka & Kubono 2011) (weak *r*-process); 2) neutron-rich matter ejected by neutron star mergers (e.g. Freiburghaus, Rosswog & Thielemann 1999; Goriely, Bauswein & Janka 2011; Wu et al. 2016) and neutron star - black hole mergers (Surman et al. 2008; Wehmeyer et al. 2019) (main *r*-process); 3) ejecta from rotating MHD core-collapse supernovae and/or collapsars (e.g. Nishimura et al. 2006; Winteler et al. 2012; Nishimura et al. 2017; Mösta et al. 2018; Siegel, Barnes & Metzger 2019). The origin of *r*-process elements in the Milky Way has been discussed recently by Côté et al. (2018b) and reviewed by Cowan et al. (2019).

The (classical) *p*-process is identified with explosive Ne/O-burning in outer zones of the progenitor star. It is initiated by the passage of the supernova shock wave and acts via photodisintegration reactions which produce neighboring (proton-rich) isotopes from pre-existing heavy nuclei (see Arnould & Goriely 2003; Rauscher et al. 2013; Pignatari et al. 2016a, and references therein). The most established scenario proposed for the *p*-process production are Type II supernova explosions (Woosley & Howard 1978; Rayet et al. 1995), with a poten-

tial relevant contribution from the advanced pre-supernova stages (Arnould 1976; Rauscher et al. 2002; Ritter et al. 2018a). Complementary scenarios are Type Ia Supernovae (Howard, Meyer & Woosley 1991; Travaglio et al. 2011, 2015; Nishimura et al. 2018) and He-accreting CO white dwarfs of sub-Chandrasekhar mass (Goriely et al. 2002). Proton-rich components of neutrino-driven winds have also been proposed as a potential relevant source for the light *p*-process nuclei (e.g. Fröhlich et al. 2006, 2017; Martínez-Pinedo, Fischer & Huther 2014; Eichler et al. 2018), although their effective contribution in the Mo and Ru region is challenged by observations of radioactive ^{92}Nb abundance in the early solar system (Dauphas et al. 2003). We refer to Pignatari et al. (2018), Wanajo et al. (2018) and Bliss, Arcones & Qian (2018) for the most up-to-date theoretical data on the production of Mo and Ru in CCSNe.

The solar abundances of Mo and Ru isotopes adopted from Anders & Grevesse (1989) are listed in the second column of Table 1. The most important isotopes contributing to the Mo and Ru abundances are ^{98}Mo and ^{102}Ru . As we mentioned before, the isotopes $^{92,94}\text{Mo}$ isotopes are produced by the *p*-process. The table also shows the *s*-process contribution to Mo isotopes derived by Travaglio et al. (2004) using GCE simulations and stellar yields for low- and intermediate-mass stars (LIM), as well as the *s*-process contribution to the solar composition estimated using the GCE simulations for Mo and Ru by Arlandini et al. (1999), Travaglio et al. (2004) and Bisterzo et al. (2014).

This paper is the last one in a series of those focused on the observations of different elements in the Galactic disc. In the first studies, particular attention was paid to the enrichment of the thin and thick disc stars with the α -elements and neutron-capture elements (Mishenina et al. 2004, 2013), as well as Mn (Mishenina et al. 2015), and Sr (Mishenina et al. 2019). Stellar observations for our sample of stars and different data sets have been compared with a number of GCE simulations (Mishenina et al. 2017). In this work, we focus on Mo and Ru. Although these elements have been investigated in metal-poor stars (e.g. Ivans et al. 2006; Peterson 2011, 2013; Roederer et al. 2012; Hansen, Andersen & Christlieb 2014; Sakari et al. 2018), there is a lack of observations at higher metallicities ($[\text{Fe}/\text{H}]$) between -0.7 and 0.3 , which is the range covered in this study. We aim at providing the first extended sample of stellar observations for Mo and Ru abundances in Galactic disc stars and analyzing their chemical signatures using theoretical GCE models.

The paper is structured as follows. The observations and selection of stars along with the definition of the main stellar parameters are described in §2. §3 presents the abundance determinations and analysis of corresponding errors. The application of the results in the theory of nucleosynthesis and the chemical evolution of the Galaxy is discussed in §4. And finally, §5 summarizes the finding and presents the conclusions drawn.

2 OBSERVATIONS AND ATMOSPHERIC PARAMETERS

In this investigation, we used the same spectra, atmospheric parameters and analytical techniques as earlier in

Table 1. Contribution of Mo and Ru isotopes to the solar abundances: 1 - Anders&Greves (1989), 2 - Arlandini et al. (1999); 3 - Travaglio et al.(2004); 4 - Bisterzo et al. (2014).

ELEMENT	SOLAR (%)	s-process (no GCE)	s-process + GCE (%)	s-process + GCE (%)	p-process (%)
	1	2	3	4	
⁹² Mo	14.84				100
⁹⁴ Mo	9.25				100
⁹⁵ Mo	15.92		39		
⁹⁶ Mo	16.68		78		
⁹⁷ Mo	9.55		46		
⁹⁸ Mo	24.13		59		
¹⁰⁰ Mo	9.63				
Mo		50	38	39	
⁹⁶ Ru	5.52				100
⁹⁸ Ru	1.88				100
⁹⁹ Ru	12.7				
¹⁰⁰ Ru	12.6				
¹⁰¹ Ru	17.0				
¹⁰² Ru	31.6				
¹⁰⁴ Ru	18.7				
Ru		32	24	29	

(Mishenina et al. 2013). The spectra of the target stars were obtained using the 1.93 m telescope at Observatoire de Haute-Provence (OHP, France) equipped with the echelle-type spectrograph ELODIE (Baranne et al. 1996) with the resolving power of $R = 42,000$, the wavelength range from 4400 to 6800 Å and signal to noise (S/N) ratio of about 100 – 300. We also used additional spectra taken from the OHP spectroscopic archive (Moultaka et al. 2004), presenting the SOPHIE spectrograph (Perruchot et al. 2008) data covering a similar wavelength range at the resolution of $R = 75,000$.

The online initial processing of spectra was carried out during observations (Katz et al. 1998). Further spectra processing such as the continuum arrangement, and measurements of the line depths and equivalent widths (EW), was conducted using the DECH30 software package developed by G.A. Galazutdinov (2007), <http://gazinur.com/DECH-software.html>.

The stellar atmospheric parameters of our target stars were determined earlier using uniform techniques for all the studied stars. The procedures employed to derive the effective temperatures T_{eff} , surface gravities $\log g$, and microturbulent velocity V_t for our stars were described in detail in Mishenina & Kovtyukh (2001) and Mishenina et al. (2004, 2008). The effective temperatures T_{eff} were derived by the calibration of the line-depth ratios for spectral line pairs that have different low-level excitation potentials (Kovtyukh et al. 2003). For the most metal-poor stars in the sample, T_{eff} were estimated by adjusting the far-wings of the H_α line (Mishenina & Kovtyukh 2001). The surface gravities $\log g$ were computed by the ionization balance, implying that similar iron abundances were obtained from the neutral iron Fe I and ionised iron Fe II lines. The microturbulent velocity V_t was established by factoring out the correlation between the abundances and the equivalent widths of the Fe I lines. We used the Fe I lines to derive the metallicity [Fe/H].

We compared our atmospheric parameters with the

results of other authors in Mishenina et al. (2004, 2008, 2013, 2019). The estimated accuracy of our parameter determinations is as follows: $\Delta T_{\text{eff}} = \pm 100$ K, surface gravities $\Delta \log g = \pm 0.2$ dex and microturbulent velocity $\Delta V_t = \pm 0.2$ km s⁻¹.

In this paper, we also compare our parameter determinations with those obtained in other studies for the stars common to our sample (Delgado Mena et al. 2017; Battistini & Bensby 2016; Adibekyan et al. 2014; Nissen & Schuster 2011; Feltzing, Fohlman & Bensby 2007; Takeda 2007; Brewer & Carney 2006; Reddy et al. 2003; Mashonkina & Gehren 2001). The mean differences between the parameters, the errors and the number of common stars are given in Table 2. In general, we see a good agreement of our findings with the results of other authors.

We adopt the kinematic classification of the stars into the thin and thick discs and Hercules stream, as described in Mishenina et al. (2013). We have not updated our classification with respect to the latest astrometric data from the Gaia Data Release 2 (Gaia Collaboration et al. 2018) because the stars in our sample are bright and tend to have Gaia astrometric errors equivalent to those of the Hipparcos observations. Some stars are even too bright to be measured by Gaia. Our previous sample (276 stars), contained 21 stars belonging to the thick disc, 212 to the thin disc, 16 to the Hercules stream, and 27 are unclassified.

3 DETERMINATION OF MO AND RU ABUNDANCES

The Mo and Ru abundances were derived using the LTE approximation applying the models of Castelli & Kurucz (2004) and the modified STARS LTE spectral synthesis code (Tsymbal 1996). For Mo I lines at 5506, 5533 Å, and Ru I lines at 4080, 4584, and 4757 Å, the oscillator strengths $\log gf$ were adopted from last version (2016)

Table 2. Comparison of obtained stellar parameters with those reported by other authors for the n stars common to our sample. The full list of stellar parameters applied for each star in this study is provided in Table A2 and in Mishenina et al. (2019).

Reference	$\Delta(T_{\text{eff}}, \text{K})$	$\Delta(\log g)$	$\Delta([\text{Fe}/\text{H}])$	n
Delgado Mena et al. (2017)	27±36	-0.08±0.13	-0.01±0.03	12
Battistini & Bensby (2016)	-4±106	-0.10±0.15	-0.03±0.06	22
Adibekyan et al. (2014)	28±57	-0.07±0.14	0.01±0.04	9
Nissen et al. (2011)	7±143	-0.03±0.20	-0.05±0.10	4
Feltzing et al. (2007)	24±76	-0.03±0.13	-0.01±0.08	10
Takeda et al. (2007)	-14±119	-0.06±0.21	-0.04±0.10	31
Brewer & Carney (2006)	64±112	0.02±0.20	0.09±0.06	4
Reddy et al. (2003)	127±13	-0.08±0.14	0.09±0.02	7
Mashonkina & Gehren (2001)	26±56	-0.10±0.21	0.03±0.06	14

of the VALD database (Kupka F. et al. 1999). Both Mo I lines are fairly well measured in the spectra of our target stars. The Mo I 5533 Å line is represented in the list of the Gaia-ESO Survey (GES), and has been used by Hansen, Andersen & Christlieb (2014) for the investigation of 71 meta-poor stars. The comparison of synthetic and observed spectra for the Mo I and Ru I lines is shown in Fig. 1.

The adopted LTE solar Mo and Ru abundances are $\log A(\text{Mo})_{\odot} = 1.88 \pm 0.08$ and $\log A(\text{Ru})_{\odot} = 1.75 \pm 0.08$ (Asplund et al. 2009).

We determined Mo abundance for 163 stars of the thin disc, 20 stars of the thick disc, 12 stars in the Hercules group, and 14 unclassified stars, which represents a total of 209 stars. Accordingly, the Ru content was determined for 124, 16, 10 and 12 stars belonging to the considered substructures, which made 162 stars in total. The obtained Mo and Ru abundances, as well as stellar parameters, are given in Table A1. Fig. 2 shows our [Mo/Fe] and [Ru/Fe] data as a function of [Fe/H].

3.1 Errors in abundance determinations

We estimated systematic errors in the abundance of molybdenum and ruthenium abundance determinations due to the uncertainty of the atmospheric parameters on the basis of the results obtained for two stars - namely, HD154345 ($T_{\text{eff}} = 5503 \text{ K}$; $\log g = 4.30$; $Vt = 1.3 \text{ km s}^{-1}$; $[\text{Fe}/\text{H}] = -0.22$) and HD82106 ($T_{\text{eff}} = 4827 \text{ K}$; $\log g = 4.10$; $Vt = 1.1 \text{ km s}^{-1}$; $[\text{Fe}/\text{H}] = -0.11$); we used the Mo, Ru abundances for several models with modified parameters ($\Delta T_{\text{eff}} = \pm 100 \text{ K}$, $\Delta \log g = \pm 0.2$, $\Delta Vt = \pm 0.1$). The obtained variations of the abundance for different parameters and the adjustment errors for the calculated and observed spectral line profiles (0.02 dex) are given in the table 3. The error in the T_{eff} determination is the major contributor to the error in the Mo and Ru abundance determinations. The total errors due to the uncertainty of the parameters and the measured spectra range from 0.12 dex for the Ru abundance to 0.16 for the Mo abundance in hotter stars. As can be seen in Figs. 3 and 4, we found no correlation between the Mo and Ru abundances and T_{eff} .

Unfortunately, no measurements of the Mo and Ru abundances in common stars have been reported elsewhere. In Table 4, we compare our atmospheric parameters and abundances of Mo and Ru with those obtained by

Hansen, Andersen & Christlieb (2014) for two stars common to our sample (Mishenina et al. 2017). Overall, the atmospheric parameters derived in both studies are consistent. For HD 22879 ($[\text{Fe}/\text{H}] \approx -1$), our upper limit for [Ru/Fe] is consistent with the actual value reported in Hansen, Andersen & Christlieb (2014).

4 RESULTS AND COMPARISON WITH THEORETICAL GCE MODELS

Hansen, Andersen & Christlieb (2014) compared the behaviour of Mo and Ru with the that of other elements, such as Sr, Zr, Pd, Ag, Ba and Eu, to detect the main sources of these elements in metal-poor stars ($[\text{Fe}/\text{H}] < -0.7$). They concluded that for the investigated range of [Fe/H], the Mo content is contributed by both the main and weak s -processes, the p -process and to a lesser extent by the main and weak r -processes. On the other hand, the Ru production is show to be correlated with Ag, suggesting the weak r -process to be the main stellar source. In this paper, the abundance measurements in F-, G-, and K-dwarfs are representative of the population of stars with higher metallicities compared to those in the sample of Hansen, Andersen & Christlieb (2014).

Fig. 5 shows the [Mo/Fe] and [Ru/Fe] abundance distribution at different [Fe/H], including our determinations for Galactic disc stars and those reported by other authors at different metallicities (Allen & Porto de Mello 2007; Peterson 2013; Hansen, Andersen & Christlieb 2014; Roederer et al. 2014; Spite et al. 2018). The Mo observations are available for a larger sample of stars at low metallicity as compared to Ru. The observational errors for Mo and Ru as follows: 0.1 dex and 0.15 dex, respectively (Peterson 2013), 0.15 dex for both Mo and Ru (this work and Hansen, Andersen & Christlieb (2014)), and 0.2 dex for both Mo and Ru (Spite et al. 2018). Roederer et al. (2014) reported data for 313 stars collected with various telescopes and spectrographs. The authors carried out a thorough analysis and processing of the adopted data, in particular, the parameter estimation, comparison of the equivalent widths obtained with different spectrographs and by different researchers, as well as application of the atmospheric models, calculation codes, line lists, etc. The comparison of the Mo and Ru abundances estimated by Roederer et al. (2014) with those obtained by other authors for all the sample stars

Table 3. Abundance errors due to the atmospheric parameter uncertainties, for two stars with different set of stellar parameters (T_{eff} , $\log g$, and Vt) - namely, HD154345 (5503, 4.30, 1.3) and HD82106 (4827, 4.10, 1.1).

		HD154345				HD82106			
AN	El	$\Delta T_{\text{eff}+}$ [K]	$\Delta \log g+$	$\Delta Vt+$ [km s ⁻¹]	tot+	$\Delta T_{\text{eff}+}$ [K]	$\Delta \log g+$	$\Delta Vt+$ [km s ⁻¹]	tot+
42	MoI	0.15	0.05	0.01	0.16	0.12	0.05	0.02	0.13
44	RuI	0.10	0.03	0.05	0.12	0.11	0.05	0.02	0.12

Table 4. Comparison of the atmospheric parameters (Mishenina et al. 2017) and Mo and Ru abundances derived in this study with the values reported in Hansen, Andersen & Christlieb (2014) for two common stars.

HD	T_{eff} [K]	$\log g$	Vt [km s ⁻¹]	[Fe/H]	[Mo/Fe] (3864 Å)	[Mo/Fe] (5506 Å)	[Ru/Fe]	reference
19445	5982	4.38	1.4	-2.13	-	-	0.7	Hansen, Andersen & Christlieb (2014)
	5830	4.00	1.1	-2.16	-	-	-	ours
22879	5792	4.29	1.2	-0.95	-	-	0.43	Hansen, Andersen & Christlieb (2014)
	5825	4.42	0.5	-0.91	-	0.45	>0.51	ours

has shown uncertainties ranging from 0.2 - 0.3 dex to 0.4 dex for Mo and Ru, respectively. Note that there are no NLTE calculations for Mo or Ru currently available. With regard to our sample of stars, since we use weak subordinate lines, and they are formed in the deep atmospheric layers wherein collisions with electrons create (establish) the LTE conditions, the NLTE corrections should be negligible and leveled using our analysis relative to the Sun. They should not make a significant contribution to the errors in the measurements reported in this paper. For more metal-poor stars, they could yield more relevant corrections. The correlations between Mo, Ru, Y, Zr, Ba, Sm, Eu (Mishenina et al. 2013), and Sr (Mishenina et al. 2019) are illustrated in Figs. 6, and Figs. A1-A3 in the Appendix. The slopes and errors obtained for our stellar sample are summarized in Table 5. We cannot deduce any detailed information from these slopes without GCE simulations representative of the disc stars. However, using the data shown in the figures, we can draw several important conclusions. The Mo and Ru abundance trends with respect to the r -process element Eu (Figs.6, A2) show no clear correlations for the thin disc stars. Moreover, the Mo enrichment does not correlate closely with Ru. Such a pattern could be associated with a late nucleosynthesis source yielding Ru, but not producing efficiently other elements in the same mass region as Mo. It is the most likely that such an extra source would not be an s -process source, since Mo and Ru have similar patterns of the s -process production (see Table 1). Having analyzed the correlation between various elements at the near solar metallicity we can derive that the galactic stellar sources which contribute to Mo and Ru content are at least partially different. Furthermore, we confirm that the contribution of the main s -process to the Mo and Ru solar abundances is lower than that for the s -process elements such, as Sr, Y and Ba. An in-depth study of the Mo and Ru production, as well as the relative impact of different stellar sources, with application of detailed GCE simulations is required. Note that the observational uncertainties are similar for Mo and Ru as discussed in the previous sections. Therefore, they cannot explain such different behaviour observed for Mo and Ru.

The application of GCE models allows us to take into account the contribution of various nucleosynthesis sources occurring at different timescales during the evolution of the elements. GCE simulations serve as a fundamental tool to understand the complex history of enrichment of elements like Mo and Ru. Recently, Prantzos et al. (2018) have carried out the investigation of the chemical evolution of the elements from H to U in the Milky Way halo and local disc. The authors used metallicity-dependent yields from low- and intermediate-mass stars (LIM, AGB), and from rotating massive stars. They found that the solar isotopic composition of pure s -process isotopes could be reproduced within 10% accuracy. They also reproduced the s -process abundances of isotopes for $90 < A < 130$ (solar LEPP Montes et al. 2007). The differences between their findings and those resulted from the GCE simulations reported by Bisterzo et al. (2017) were mainly due to the yields adopted for rotating massive stars, in particular, Prantzos et al. (2018) used the isotopic yields from Limongi & Chieffi (2018). Moreover, the AGB yields used in both studies were not similar that could affect the results obtained for the elements which are subject to our study. Prantzos et al. (2018) have also concluded that there are significant differences at lower [Fe/H] for which the chemical evolution is mainly governed by massive stars and emphasized some deficiency in Zr and Mo.

Our new observational data for Mo and Ru along with those reported by Hansen, Andersen & Christlieb (2014); Peterson (2013); Roederer et al. (2014); Spite et al. (2018) are presented in Figs. 7 and 8, respectively. The bottom panels in the figures illustrate the evolution of Mo and Ru for the metallicity range of the Galactic disc. The GCE evolution of Mo predicted by Prantzos et al. (2018) (as presented in Fig.16 in their study) is compared with the observational data in Fig. 7. As also highlighted by the authors, the theoretical trends are not reproducing the Galactic behavior of Mo: GCE simulations do not produce enough Mo compared to Fe in comparison to observations. Fig. 7 also shows the GCE results of Bisterzo et al. (2017), who used the same chemical evolution model as Travaglio et al. (2004). The

Table 5. Elemental abundance trends related to Mo and Ru, as shown in Figs. 6, A1, A2, A3, for thin disc stars (3rd column) and thick disc stars (4th column).

1	2	3	4
Element	Reference	Slope \pm Error	Slope \pm Error
Ru	Mo	0.49 ± 0.06	0.76 ± 0.14
Ba	Mo	1.16 ± 0.09	1.23 ± 0.13
Ba	Ru	0.99 ± 0.15	1.32 ± 0.26
Sr	Y	1.17 ± 0.04	1.07 ± 0.04
Sr	Mo	1.48 ± 0.08	1.36 ± 0.12
Sr	Ru	1.15 ± 0.16	1.30 ± 0.30
Y	Mo	0.97 ± 0.08	1.27 ± 0.11
Zr	Mo	0.83 ± 0.08	0.97 ± 0.08
Sm	Mo	0.67 ± 0.06	1.06 ± 0.10
Sm	Ru	0.64 ± 0.09	1.17 ± 0.19
Eu	Mo	0.60 ± 0.06	0.84 ± 0.11
Eu	Ru	0.43 ± 0.10	0.80 ± 0.17

latter prediction for $[\text{Mo}/\text{Fe}]$ assumed 40% s -process contribution from AGB stars (see Bisterzo et al. 2017, for details), 10% contribution from the r -process, and 1% contribution from the weak s -component from massive stars. We also obtained 49% contribution from LEPP (derived from Travaglio et al. (2004)). As in Travaglio et al. (2015), we can also derive separately the p -process contribution to the two p -only isotopes of Mo, i.e. $^{92,94}\text{Mo}$ from Type Ia supernovae (a single degenerate scenario). However, the p -process contribution to the total Mo abundance is irrelevant for reproducing the Mo observations in the Galaxy.

In Figs. 7 and 8 we also show the evolution of $[\text{Mo}/\text{Fe}]$ and $[\text{Ru}/\text{Fe}]$, as predicted using the open-source GCE code OMEGA+ (Côté et al. 2018c), which is part of the JINAPyCEE Python package¹. This is a two-zone model consisting of a classical one-zone chemical evolution model located at the center of a large gas reservoir (the circumgalactic medium of the simulated galaxy). For low- and intermediate-mass stars, we used the stellar yields reported in Cristallo et al. 2015 with no rotation and standard ^{13}C pocket, which are available with the the F.R.U.I.T.Y² database. For thermonuclear supernovae (SNIa), we adopted the yields from Iwamoto et al. (1999) and distributed them in time following a function based on the observed delay-time distribution function for SNIa (see Côté et al. 2016 and Ritter et al. 2018b for more details). For the CCSNe yields, we used the NuGrid massive star models (Ritter et al. 2018c) along with the *delayed* supernova engine prescription (Fryer et al. 2012). In order to calculate the integrated stellar yields used in the GCE simulations, we did not use the $12 M_{\odot}$ models at all metallicities. The SN explosion setup used for these models causes an overproduction of Fe abundances when compared to the solar composition, which indicates that the conditions obtained are not representative of those in most of $12 M_{\odot}$ CCSNe do (see, Côté et al. 2018a; Philcox, Rybizki & Gutcke 2018). We also did not consider the $15 M_{\odot}$ model at $Z = 0.006$. That single model included a strong α -rich freezeout contribution (e.g.

Woosley & Hoffman 1992; Pignatari et al. 2016b), that resulted in the overestimated GCE production for some first-peak neutron-capture elements, such as Y and Zr, in our simulations. Therefore, the α -rich freezeout component obtained in that model is not representative of what $15 M_{\odot}$ CCSNe stars typically produce. For the GCE models considered below, for simplicity, we replaced the $15 M_{\odot}$ model at $Z = 0.006$ with the $15 M_{\odot}$ model at $Z = 0.001$, without causing any impact on the GCE of Mo and Ru. The only difference between the two OMEGA+ models presented in Figs. 7 and 8, is a different setup for the r -process production. For both models, the dominant r -process source are neutron star mergers (e.g. Cowan et al. 2019; Côté et al. 2019). However, for each r -process event we assume that the ejecta is released either 30 Myr after the formation of the progenitor star (short-delay time setup), or released following a delay-time distribution function in the form of t^{-1} from 10 Myr to 10 Gyr (delay-time distribution setup) (Chruslinska et al. 2018).

As can be seen in the bottom panel of Fig. 7, the contribution from massive rotating stars or from AGB stars at higher metallicities does not solve the issue of underproduction in theoretical predictions as compared to the observations (Prantzos et al. 2018). The simulations by Travaglio et al. (2004) and OMEGA+ (short delay time setup) seem to show a better consistency with Mo observations, reducing the average underproduction to about 0.1 dex. For the data reported in Travaglio et al. (2004) this might be due to the additional contribution to Mo by the Lighter Element Primary Process component, considered in these GCE models. Concerning OMEGA+ results, the difference is mainly due to the r -process sources different from those in two other sets of GCE simulations. In particular, the yields of neutron-star mergers are implemented as decoupled with CCSNe which is the main source of Fe at low metallicity.

According to the results of our comparison of the OMEGA+ and Travaglio et al. (2004) more thoroughly, the s -process contribution to the solar abundances of Mo and Ru is 60% and 45%, respectively, which is different from 40% and 24% obtained by Travaglio et al. (2004). The r -process contribution obtained is 16% and 45% respectively, compared to 12% and 50% derived from the elemental distri-

¹ <https://github.com/becot85/JINAPyCEE>

² <http://fruity.oa-teramo.inaf.it/modelli.pl>

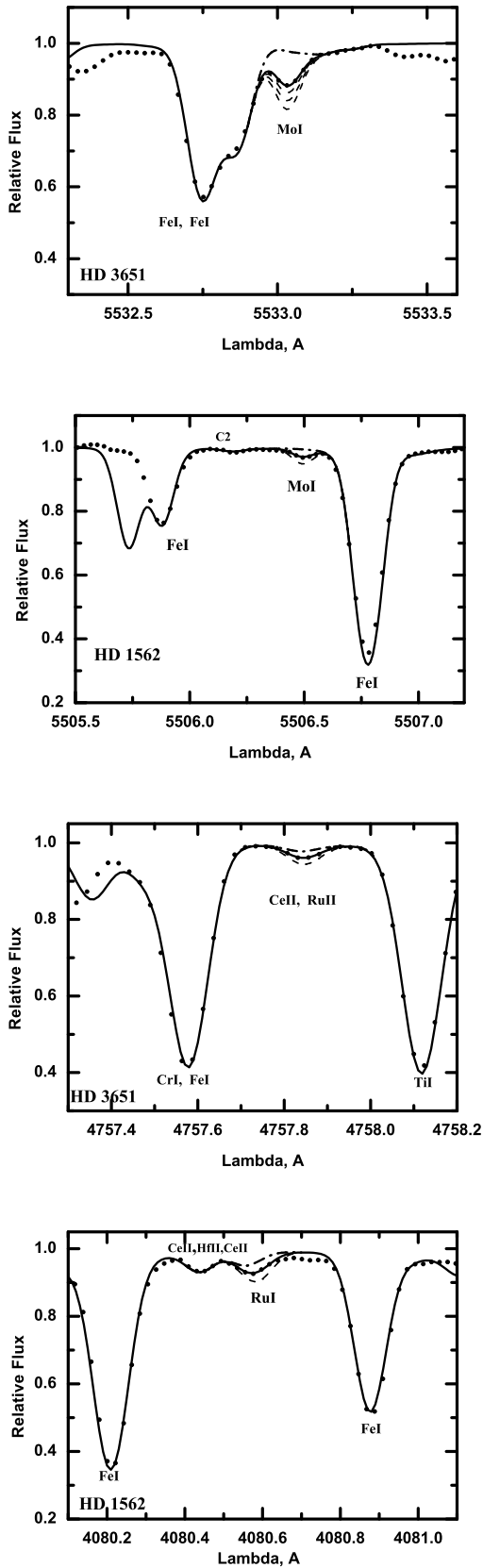


Figure 1. Observed (dotted) and calculated (solid) spectra in the region of Mo I and Ru I lines for the stars HD 1562 and HD 3651. The dashed lines correspond to the difference in 0.1 dex for the Mo abundance in HD 3651 and 0.3 dex in other cases.

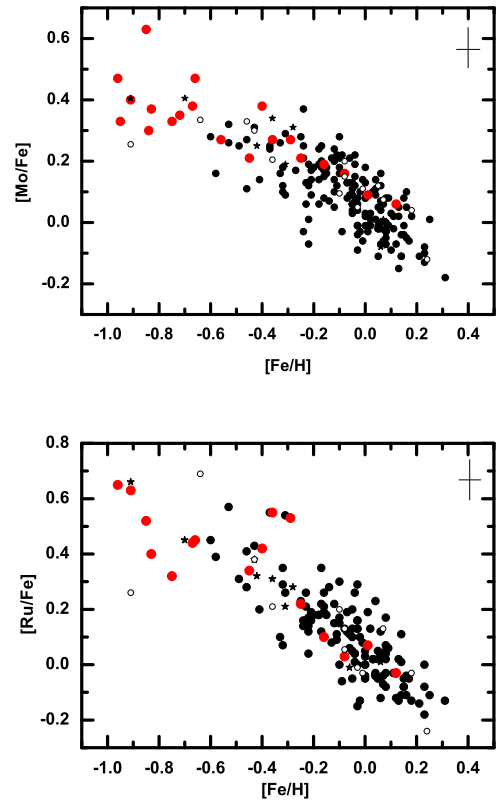


Figure 2. $[\text{Mo}/\text{Fe}]$ and $[\text{Ru}/\text{Fe}]$ as a function of $[\text{Fe}/\text{H}]$. The stars belonging to the thin and thick discs are marked with small black and red circles, respectively. The stars classified into the Hercules stream are marked with asterisks while non-classified stars are depicted as open circles. The error bar is marked with a cross in the upper-right corner.

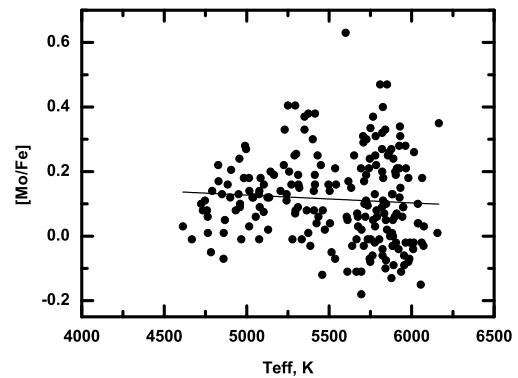


Figure 3. Dependence of $[\text{Mo}/\text{Fe}]$ on T_{eff} .

bution of the r -process in the metal-poor star CS 22892-052 and used as a reference of the r -process contribution in Travaglio et al. (2004). Despite such a higher s -process contribution obtained in OMEGA+ calculations, the requirement for having additional sources for Mo at low metallicity is consistent with the results of other GCE simulations referred to in this paper. Concerning Ru, the two OMEGA+ models show

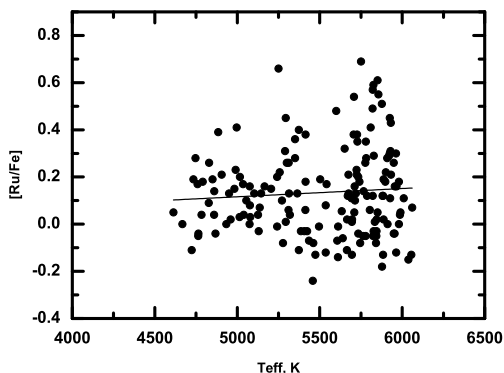


Figure 4. Dependence of $[Ru/Fe]$ on T_{eff} .

different results with a higher $[Ru/Fe]$ trend using the short delay time setup. On the other hand, even in the most optimistic conditions, at metallicities lower than solar ones, the GCE model yield is 0.2 dex lower as compared to the observations.

Despite the fact that the r -process contributes to a small fraction of the solar Mo, and a half of that of Ru, it becomes more significant at low metallicities, where the s -process contribution from AGB stars becomes marginal. In particular, we show in the bottom panels of Figs. 7 and 8 that the properties of the r -process sources adopted in the GCE simulations have a strong impact on the abundances of Mo and Ru for $[Fe/H] < -0.2$ dex, if we assume that all r -process events carry a solar r -process residual pattern for the yields (e.g. Arnould, Goriely & Takahashi 2007). In a more general sense, the study of the chemical evolution of these elements can provide additional new constraints on the r -process production in the Galaxy and other nucleosynthesis processes active in the early Galaxy. In Fig. 9, we show that while $[Mo/Eu]$ is consistent within 0.4 dex in our stellar sample, the observed scatter increases up to about 2 dex in more metal poor stars (Hansen, Andersen & Christlieb 2014). This would imply that at least Mo-poor and Mo-rich nucleosynthesis sources with respect to Eu were active in the early Galaxy. At the same time, the $[Mo/Fe]$ and $[Ru/Fe]$ scatter observed at low metallicities (see Fig. 5) is quite similar to that of $[Eu/Fe]$, indicating that also the production of Mo and Ru with respect to Fe at low metallicity is associated to rare events. A detailed study of these observations for $[Fe/H] \lesssim -2$ would possibly require an inhomogeneous galactic chemical evolution study (e.g. Wehmeyer, Pignatari & Thielemann 2015; Mishenina et al. 2017).

5 CONCLUSIONS

We presented new observational data for the light trans-Fe elements Mo ($Z = 42$) and Ru ($Z = 44$) in F-, G-, and K-stars belonging to the substructures of the Galaxy with metallicities ranging from $-1.0 < [Fe/H] < +0.3$. The spectra of Galactic disc stars have a high resolution of 42,000 and 75,000 and signal-to-noise ratio better than 100. The Mo and Ru abundances were derived by comparing the observed and

synthetic spectra in the region of Mo I lines at 5506, 5533 Å (for 209 stars), and Ru I lines at 4080, 4584, and 4757 Å (for 162 stars) in the LTE approximation. For all the stars the Mo and Ru abundance determinations were obtained for the first time. Taking into consideration the observational data reported in other studies at low metallicities, this work enables us to analyse the complete trend of Mo and Ru abundances in the Milky Way.

As follows from the observations at lower metallicities, the existing GCE models with the nucleosynthesis sites and stellar yields included therein underproduce Mo and Ru compared to observational data also in the Galactic disc. Canonical stellar sources of heavy elements, such as the s -process in massive stars and AGB stars or the r -process, do not appear to produce sufficient amount of these elements. Factoring in the additional Lighter Element Primary Process or LEPP in GCE simulations allows to obtain a better fit. However, the nature and the origin of LEPP is still a matter for debate, and such a zoo of numerous independent stellar processes could contribute instead to the production of various elements. According to the GCE models presented in this paper, also the assumption of an r -process source disentangled by CCSNe like neutron star mergers can provide in principle a better fit for the observations. However, even the most Mo-rich and Ru-rich GCE simulations cannot reproduce all the observed Mo and Ru. Similar indications seem to be obtained for metal-poor stars, but hydrodynamics chemical evolution or inhomogeneous chemical evolution models are needed in order to study the inhomogeneous enrichment of the galactic halo.

In summary, the origin of the two elements remains an open question requiring further detailed studying. We found that some other stellar sites and their contributions should be included in the GCE calculations, apart from the classical nucleosynthesis processes. As regards Eu, the large scatter observed for $[Mo/Fe]$ and $[Ru/Fe]$ at low metallicities would be consistent with the contribution from a rare stellar source. For the thick and thin disc stars in our sample, we found that the Mo enrichment is correlated with both Ba and Eu. On the other hand, Ru shows a much higher dispersion with respect to Mo, Ba and Eu. A possible scenario that we suggested and discussed is that Ru could be efficiently produced by an extra stellar nucleosynthesis source active in the Galactic disc. Further investigation with GCE simulations is required to better define the nature of such a source. Today, we can only argue that it is not an s -process source, since the s -process contributions to Mo and Ru are similar. At present, spectroscopic abundance measurements available for Mo and Ru are based on the LTE calculations with no NLTE corrections currently available. Though it should not be an issue within the metallicity range of our stellar sample, more significant corrections could be required for the observations in metal-poor stars. However, since the discrepancy between theoretical predictions and observations is already evident from the simulations of the chemical evolution of the Milky Way disc, it would not affect the main findings and conclusions presented in this paper

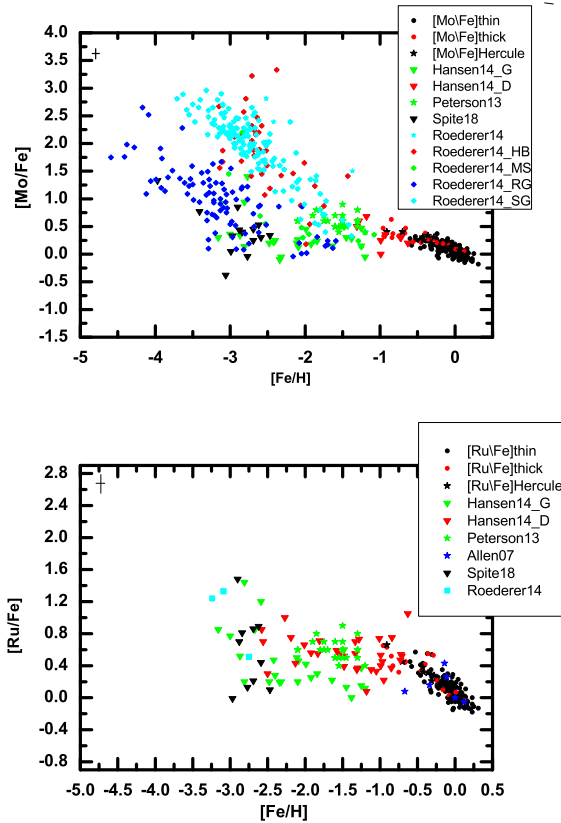


Figure 5. Observed $[\text{Mo}/\text{Fe}]$ (top panel) and $[\text{Ru}/\text{Fe}]$ (bottom panel) as a function of $[\text{Fe}/\text{H}]$ resulted from the comparison of our sample of stellar data with those reported by other authors. Symbols are specified in the figure: Hansen14-G and Hansen14-D refer to giant and dwarf stars by Hansen, Andersen & Christlieb (2014); Peterson13 are stars by Peterson (2013); Spite18 by Spite et al. (2018), Roderer14-HB, Roederer14-MS, Roderer14-RG and Roderer14-SG are respectively Horizontal Branch, Main Sequence, Red Giant and Subgiant branch stars by Roederer et al. (2014); Allen07 refers to Allen & Porto de Mello (2007). The average of the observational errors is provided in the upper left corner.

ACKNOWLEDGEMENTS

This paper was based on the observation data collected at OHP Observatory, France. TM, TG, MP, FKT grateful for the support from the Swiss National Science Foundation, project SCOPES No. IZ73Z0152485. MP acknowledges significant support to NuGrid from NSF grant PHY-1430152 (JINA Center for the Evolution of the Elements) and STFC (through the University of Hull’s Consolidated Grant ST/R000840/1), and access to VIPER, the University of Hull High Performance Computing Facility. MP acknowledges the support from the “Lendlet-2014” Programme of the Hungarian Academy of Sciences (Hungary), and from the BRIDGCE UK network. FKT acknowledges support from the European Research Council (FP7) under ERC Advanced Grant Agreement 321263 FISH. BC and MP acknowledges support from the ERC Consolidator Grant (Hungary) funding scheme (project RADIOSTAR, G.A. n. 724560) and from the National Science Foundation (USA) under grant No. PHY-1430152 (JINA Center for the Evolution of the Elements). This article is based upon work from the ChETEC COST Action (CA16117), supported by COST (European Cooperation in Science and Technology). TM thanks to S. Korotin for discussions. The authors ap-

preciate very useful comments provided by the anonymous referee.

REFERENCES

- Adibekyan V. Z., González Hernández J. I., Delgado Mena E., Sousa S. G., Santos N. C., Israelian G., Figueira P., Bertran de Lis S., 2014, *A&A*, 564, L15
- Allen D. M., Porto de Mello G. F., 2007, *A&A*, 474, 221
- Anders E., Grevesse N., 1989, *Geochim. Cosmochim. Acta*, 53, 197
- Arcones A., Montes F., 2011, *ApJ*, 731, 5
- Arlandini C., Käppeler F., Wisshak K., Gallino R., Lugaro M., Busso M., Straniero O., 1999, *ApJ*, 525, 886
- Arnould M., 1976, *A&A*, 46, 117
- Arnould M., Goriely S., 2003, *Phys. Rep.*, 384, 1
- Arnould M., Goriely S., Takahashi K., 2007, *Phys. Rep.*, 450, 97
- Asplund M., Grevesse N., Sauval A. J., Scott P., 2009, *ARA&A*, 47, 481
- Baranne A. et al., 1996, *A&AS*, 119, 373
- Battistini C., Bensby T., 2016, *A&A*, 586, A49
- Bisterzo S., Travaglio C., Gallino R., Wiescher M., Käppeler F., 2014, *ApJ*, 787, 10

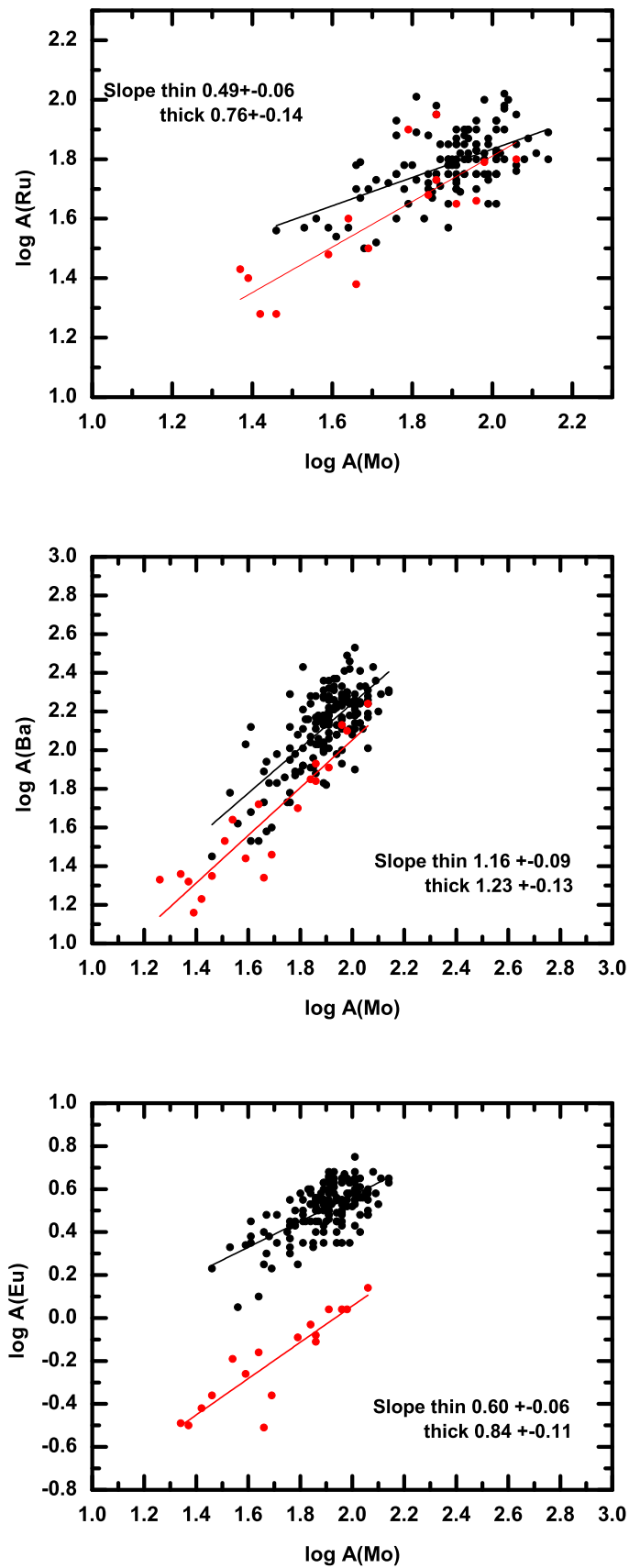


Figure 6. Trends of $\log A(\text{El})$ where $\text{El} = \text{Ru}, \text{Ba}, \text{and Eu}$ vs. $\log A(\text{Mo})$ for thin disc stars (small black circles) and thick disc stars (red circles).

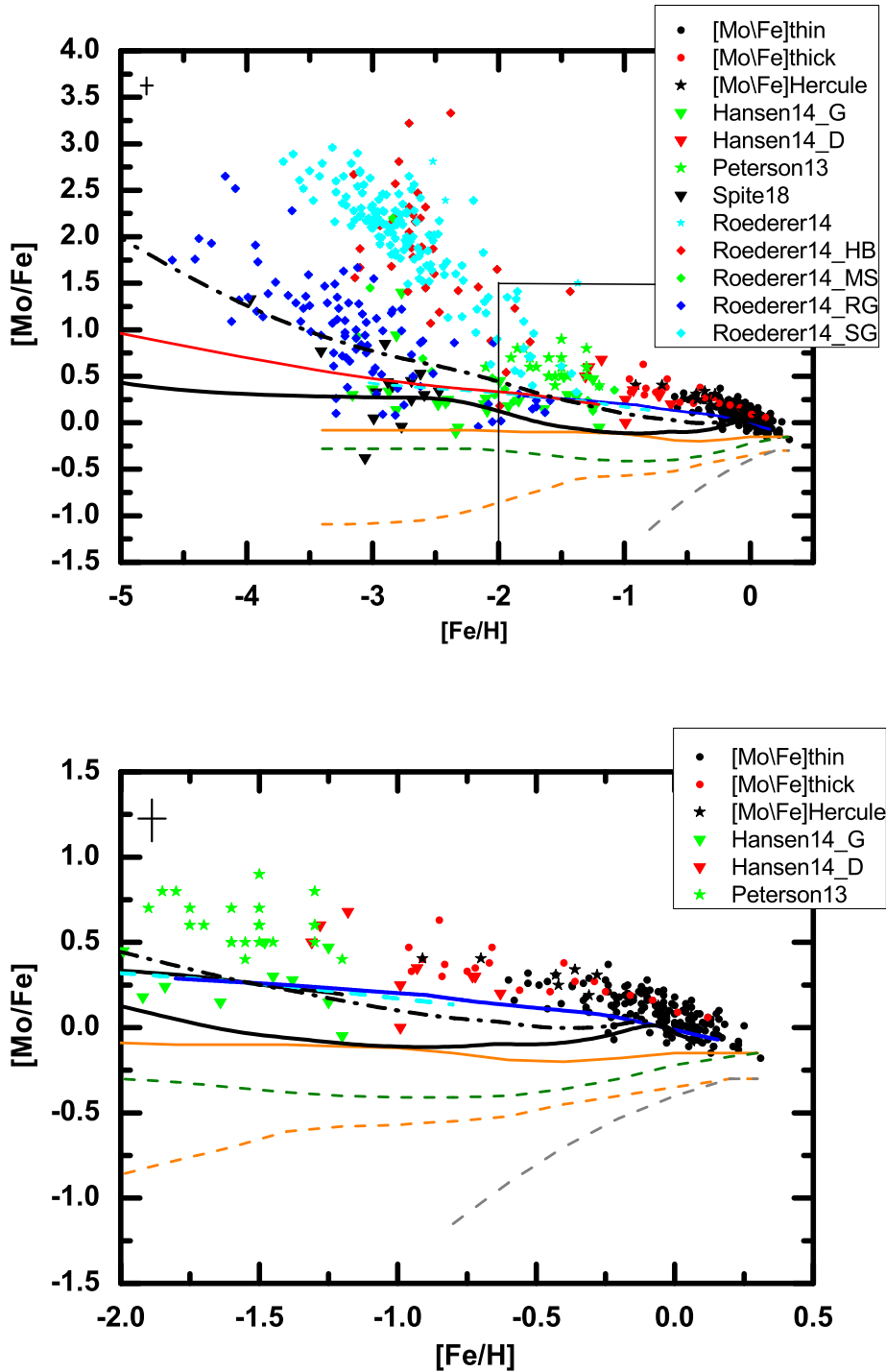


Figure 7. Top Panel: evolution of $[\text{Mo}/\text{Fe}]$ as a function of $[\text{Fe}/\text{H}]$ predicted by the chemical evolution models of Prantzos et al. (2018) and Travaglio et al. (2004) as compared to the observation data (markers are specified in the figure). For Prantzos et al. (2018) simulations, the following models are shown: i) LIM stars, rotating massive stars plus their fiduciary r -process (the baseline model, orange solid curve); ii) LIM stars, non-rotating massive stars and r -process (green dashed curve); iii) LIM stars and non-rotating massive stars without r -process contribution (gray dashed curve); and iv) LIM stars plus rotating massive stars without the r -process contribution (orange dashed curve). For the Travaglio et al. (2004) predictions, the models for halo, thick and thin disc of the Milky Way are reported (solid red, dashed cyan and solid blue curves, respectively). The curves overlap within the metallicity range $-2 < [\text{Fe}/\text{H}] < -1$. The prediction by the OMEGA+ code, short delay time (r -process) and delay time distribution (r -process) marked as black dots - dashed line and solid line, respectively. Bottom panel: the same as on the top panel, but for the metallicity range of the Galactic disc. The average observational errors is provided in the upper-left corner.

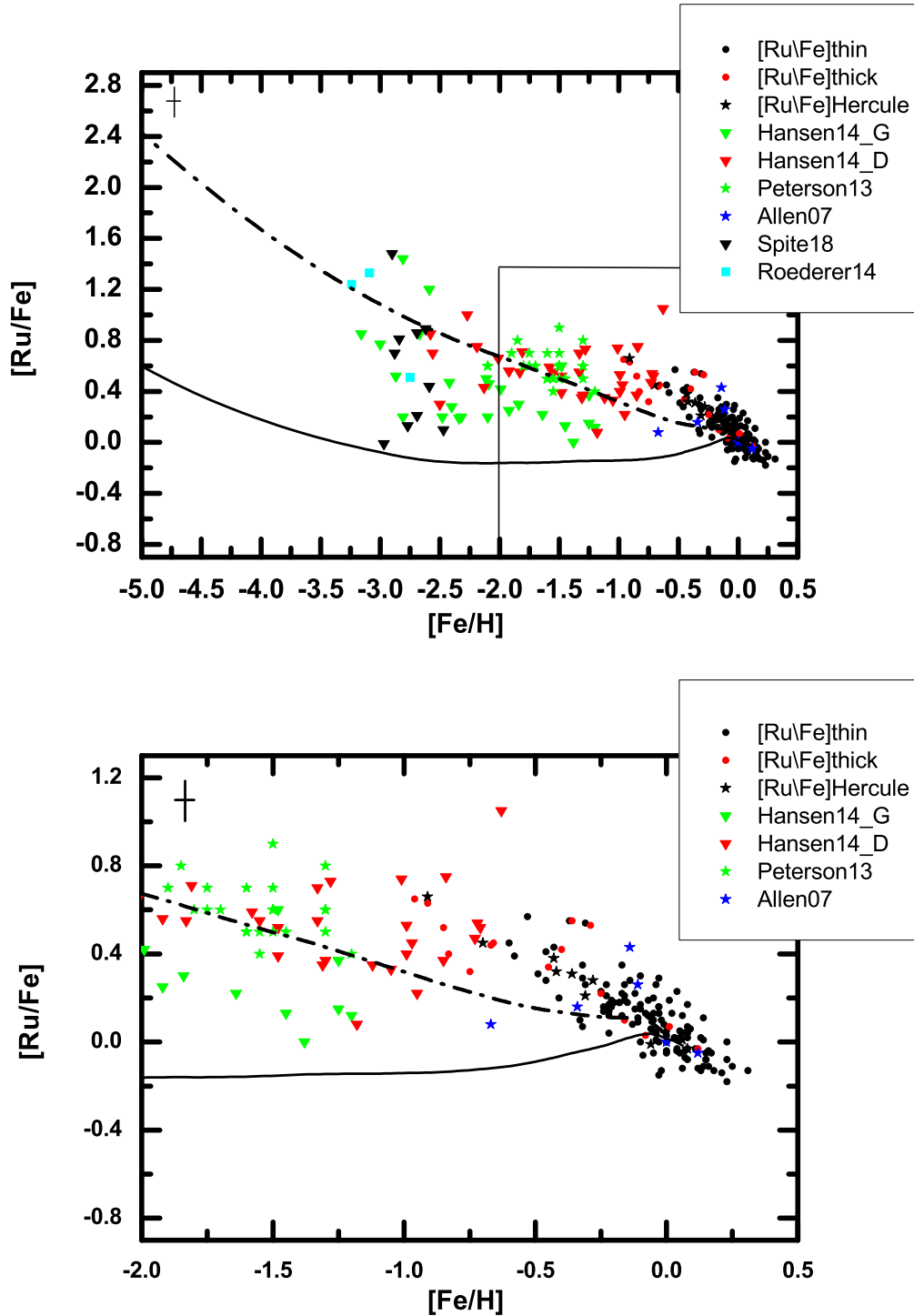


Figure 8. Top panel: evolution of $[Ru/Fe]$ as a function of $[Fe/H]$ predicted by the OMEGA+ code, the short delay time (r -process) and delay time distribution (r -process) marked with black dot, dashed and solid line, respectively, as compared to the observational data (markers are specified in the figure). Bottom panel: the same as on the top panel, but for the metallicity range of the Galactic disc. The average observational errors is provided in the upper-left corner.

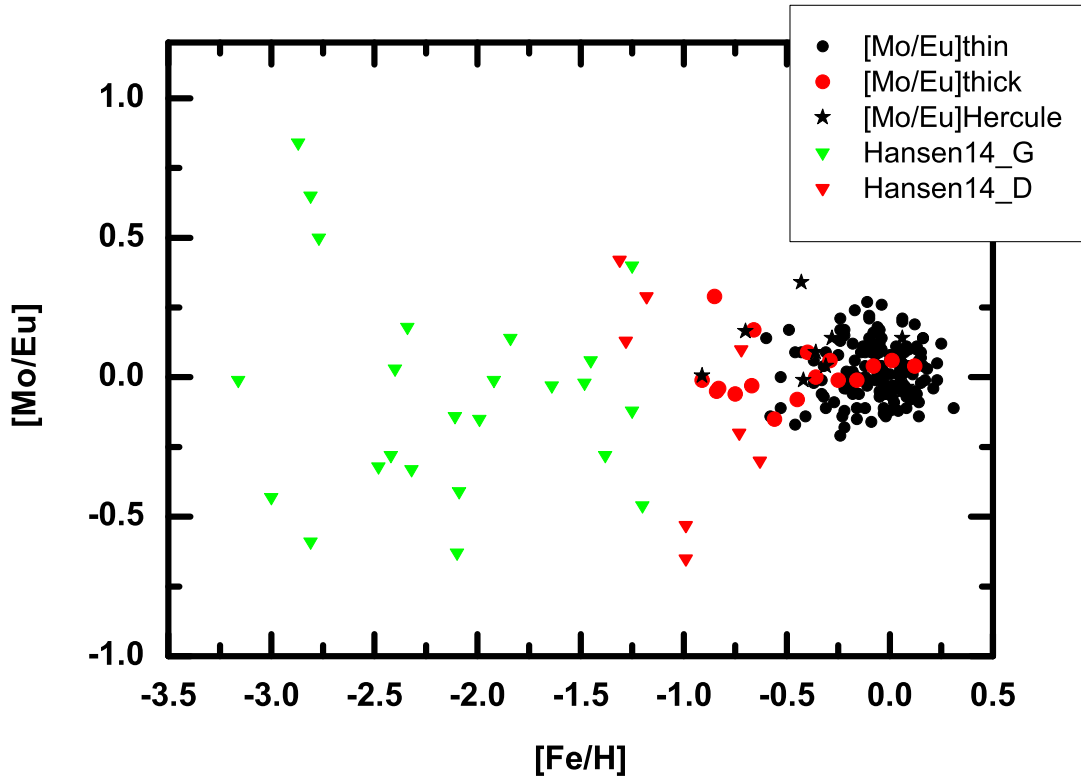


Figure 9. Evolution of $[\text{Mo}/\text{Eu}]$ as a function of $[\text{Fe}/\text{H}]$.

- Bisterzo S., Travaglio C., Wiescher M., Käppeler F., Gallino R., 2017, *ApJ*, 835, 97
- Bliss J., Arcones A., Qian Y.-Z., 2018, *ApJ*, 866, 105
- Brewer M.-M., Carney B. W., 2006, *AJ*, 131, 431
- Busso M., Gallino R., Wasserburg G. J., 1999, *ARA&A*, 37, 239
- Castelli F., Kurucz R. L., 2004, *ArXiv Astrophysics e-prints*, astro-ph/0405087
- Cescutti G., Romano D., Matteucci F., Chiappini C., Hirschi R., 2015, *A&A*, 577, A139
- Chopin A., Hirschi R., Meynet G., Ekström S., Chiappini C., Laird A., 2018, *A&A*, 618, A133
- Chruslinska M., Belczynski K., Klencki J., Benacquista M., 2018, *MNRAS*, 474, 2937
- Côté B., Denissenkov P., Herwig F., Ruiter A. J., Ritter C., Pignatari M., Belczynski K., 2018a, *ApJ*, 854, 105
- Côté B. et al., 2019, *ApJ*, 875, 106
- Côté B. et al., 2018b, *ApJ*, 855, 99
- Côté B., Ritter C., O'Shea B. W., Herwig F., Pignatari M., Jones S., Fryer C. L., 2016, *ApJ*, 824, 82
- Côté B., Silvia D. W., O'Shea B. W., Smith B., Wise J. H., 2018c, *ApJ*, 859, 67
- Cowan J. J., Rose W. K., 1977, *ApJ*, 217, 51
- Cowan J. J., Sneden C., Lawler J. E., Aprahamian A., Wiescher M., Langanke K., Martínez-Pinedo G., Thielemann F.-K., 2019, *arXiv e-prints* 1901.01410
- Cristallo S., Straniero O., Piersanti L., Gobrecht D., 2015, *ApJS*, 219, 40
- Dauphas N., Rauscher T., Marty B., Reisberg L., 2003, *Nuclear Physics A*, 719, C287
- Delgado Mena E., Tsantaki M., Adibekyan V. Z., Sousa S. G., Santos N. C., González Hernández J. I., Israelian G., 2017, *A&A*, 606, A94
- Eichler M. et al., 2018, *Journal of Physics G Nuclear Physics*, 45, 014001
- Farouqi K., Kratz K.-L., Mashonkina L. I., Pfeiffer B., Cowan J. J., Thielemann F.-K., Truran J. W., 2009, *ApJ*, 694, L49
- Feltzing S., Fohlman M., Bensby T., 2007, *A&A*, 467, 665
- Freiburghaus C., Rosswog S., Thielemann F.-K., 1999, *ApJ*, 525, L121
- Frischknecht U. et al., 2016, *MNRAS*, 456, 1803
- Fröhlich C., Hatcher D., Perdikakis G., Nikas S., 2017, in 14th International Symposium on Nuclei in the Cosmos (NIC2016), Kubono S., Kajino T., Nishimura S., Isobe T., Nagataki S., Shima T., Takeda Y., eds., p. 010505
- Fröhlich C., Martínez-Pinedo G., Liebendörfer M., Thielemann F.-K., Bravo E., Hix W. R., Langanke K., Zinner N. T., 2006, *Physical Review Letters*, 96, 142502
- Fryer C. L., Belczynski K., Wiktorowicz G., Dominik M., Kalogera V., Holz D. E., 2012, *ApJ*, 749, 91
- Gaia Collaboration et al., 2018, *A&A*, 616, A11
- Gallino R., Arlandini C., Busso M., Lugaro M., Travaglio C., Straniero O., Chieffi A., Limongi M., 1998, *ApJ*, 497, 388
- Goriely S., Bauswein A., Janka H.-T., 2011, *ApJ*, 738, L32
- Goriely S., José J., Hernanz M., Rayet M., Arnould M., 2002, *A&A*, 383, L27

- Hansen C. J., Andersen A. C., Christlieb N., 2014, *A&A*, 568, A47
- Herwig F., 2005, *ARA&A*, 43, 435
- Hoffman R. D., Woosley S. E., Fuller G. M., Meyer B. S., 1994, in *Bulletin of the American Astronomical Society*, Vol. 26, American Astronomical Society Meeting Abstracts, p. 1363
- Hoffman R. D., Woosley S. E., Qian Y.-Z., 1997, *ApJ*, 482, 951
- Howard W. M., Meyer B. S., Woosley S. E., 1991, *ApJ*, 373, L5
- Ivans I. I., Simmerer J., Sneden C., Lawler J. E., Cowan J. J., Gallino R., Bisterzo S., 2006, *ApJ*, 645, 613
- Iwamoto K., Brachwitz F., Nomoto K., Kishimoto N., Umeda H., Hix W. R., Thielemann F.-K., 1999, *ApJS*, 125, 439
- Käppeler F., Gallino R., Bisterzo S., Aoki W., 2011, *Reviews of Modern Physics*, 83, 157
- Karakas A. I., Lattanzio J. C., 2014, *PASA*, 31, e030
- Katz D., Soubiran C., Cayrel R., Adda M., Cautain R., 1998, *A&A*, 338, 151
- Kovtyukh V. V., Soubiran C., Belik S. I., Gorlova N. I., 2003, *A&A*, 411, 559
- Kratz K.-L., Farouqi K., Möller P., 2014, *ApJ*, 792, 6
- Kupka F., Piskunov N.E., Ryabchikova T.A., Stempels H. C., Weiss W. W., 1999, *A&AS*, 138
- Limongi M., Chieffi A., 2018, *ApJS*, 237, 13
- Maeder A., Meynet G., Chiappini C., 2015, *A&A*, 576, A56
- Martínez-Pinedo G., Fischer T., Huther L., 2014, *Journal of Physics G Nuclear Physics*, 41, 044008
- Mashonkina L., Gehren T., 2001, *A&A*, 376, 232
- Mishenina T., Gorbaneva T., Pignatari M., Thielemann F.-K., Korotin S. A., 2015, *MNRAS*, 454, 1585
- Mishenina T. et al., 2017, *MNRAS*, 469, 4378
- Mishenina T., Pignatari M., Gorbaneva T., Bisterzo S., Travaglio C., Thielemann F.-K., Soubiran C., 2019, *MNRAS*, 484, 3846
- Mishenina T. V., Kovtyukh V. V., 2001, *A&A*, 370, 951
- Mishenina T. V., Pignatari M., Korotin S. A., Soubiran C., Charbonnel C., Thielemann F.-K., Gorbaneva T. I., Basak N. Y., 2013, *A&A*, 552, A128
- Mishenina T. V., Soubiran C., Bienaymé O., Korotin S. A., Belik S. I., Usenko I. A., Kovtyukh V. V., 2008, *A&A*, 489, 923
- Mishenina T. V., Soubiran C., Kovtyukh V. V., Korotin S. A., 2004, *A&A*, 418, 551
- Montes F. et al., 2007, *ApJ*, 671, 1685
- Mösta P., Roberts L. F., Halevi G., Ott C. D., Lippuner J., Haas R., Schnetter E., 2018, *ApJ*, 864, 171
- Moultaka J., Ilovaisky S. A., Prugniel P., Soubiran C., 2004, *PASP*, 116, 693
- Nishimura N., Rauscher T., Hirschi R., Murphy A. S. J., Cescutti G., Travaglio C., 2018, *MNRAS*, 474, 3133
- Nishimura N., Sawai H., Takiwaki T., Yamada S., Thielemann F.-K., 2017, *ApJ*, 836, L21
- Nishimura S., Kotake K., Hashimoto M.-a., Yamada S., Nishimura N., Fujimoto S., Sato K., 2006, *ApJ*, 642, 410
- Nissen P. E., Schuster W. J., 2011, *A&A*, 530, A15
- Perruchot S. et al., 2008, in *Proc. SPIE*, Vol. 7014, *Ground-based and Airborne Instrumentation for Astronomy II*, p. 70140J
- Peterson R. C., 2011, *ApJ*, 742, 21
- Peterson R. C., 2013, *ApJ*, 768, L13
- Philcox O., Rybizki J., Gutcke T. A., 2018, *ApJ*, 861, 40
- Pignatari M., Gallino R., Heil M., Wiescher M., Käppeler F., Herwig F., Bisterzo S., 2010, *ApJ*, 710, 1557
- Pignatari M., Gallino R., Meynet G., Hirschi R., Herwig F., Wiescher M., 2008, *ApJ*, 687, L95
- Pignatari M., Göbel K., Reifarth R., Travaglio C., 2016a, *International Journal of Modern Physics E*, 25, 1630003
- Pignatari M. et al., 2016b, *ApJS*, 225, 24
- Pignatari M., Hoppe P., Trappitsch R., Fryer C., Timmes F. X., Herwig F., Hirschi R., 2018, *Geochim. Cosmochim. Acta*, 221, 37
- Prantzos N., Abia C., Limongi M., Chieffi A., Cristallo S., 2018, *MNRAS*, 476, 3432
- Rauscher T., Dauphas N., Dillmann I., Fröhlich C., Fülöp Z., Gyürky G., 2013, *Reports on Progress in Physics*, 76, 066201
- Rauscher T., Heger A., Hoffman R. D., Woosley S. E., 2002, *ApJ*, 576, 323
- Rayet M., Arnould M., Hashimoto M., Prantzos N., Nomoto K., 1995, *A&A*, 298, 517
- Reddy B. E., Tomkin J., Lambert D. L., Allende Prieto C., 2003, *MNRAS*, 340, 304
- Ritter C., Andrassy R., Côté B., Herwig F., Woodward P. R., Pignatari M., Jones S., 2018a, *MNRAS*, 474, L1
- Ritter C., Côté B., Herwig F., Navarro J. F., Fryer C. L., 2018b, *ApJS*, 237, 42
- Ritter C., Herwig F., Jones S., Pignatari M., Fryer C., Hirschi R., 2018c, *MNRAS*, 480, 538
- Roederer I. U. et al., 2012, *ApJS*, 203, 27
- Roederer I. U., Preston G. W., Thompson I. B., Shectman S. A., Sneden C., Burley G. S., Kelson D. D., 2014, *AJ*, 147, 136
- Sakari C. M. et al., 2018, *ApJ*, 854, L20
- Siegel D. M., Barnes J., Metzger B. D., 2019, *Nature*, 569, 241
- Spite F., Spite M., Barbuy B., Bonifacio P., Caffau E., François P., 2018, *A&A*, 611, A30
- Straniero O., Gallino R., Busso M., Chieffi A., Raiteri C. M., Limongi M., Salaris M., 1995, *ApJ*, 440, L85
- Surman R., McLaughlin G. C., Ruffert M., Janka H.-T., Hix W. R., 2008, *ApJ*, 679, L117
- Takeda Y., 2007, *PASJ*, 59, 335
- The L.-S., El Eid M. F., Meyer B. S., 2007, *ApJ*, 655, 1058
- Travaglio C., Gallino R., Arnone E., Cowan J., Jordan F., Sneden C., 2004, *ApJ*, 601, 864
- Travaglio C., Gallino R., Rauscher T., Röpke F. K., Hillebrandt W., 2015, *ApJ*, 799, 54
- Travaglio C., Röpke F. K., Gallino R., Hillebrandt W., 2011, *ApJ*, 739, 93
- Tsymbal V., 1996, 108, 198
- Wanajo S., Janka H.-T., Kubono S., 2011, *ApJ*, 729, 46
- Wanajo S., Kajino T., Mathews G. J., Otsuki K., 2001, *ApJ*, 554, 578
- Wanajo S., Müller B., Janka H.-T., Heger A., 2018, *ApJ*, 852, 40
- Wehmeyer B., Fröhlich C., Côté B., Pignatari M., Thielemann F.-K., 2019, *MNRAS*, 487, 1745
- Wehmeyer B., Pignatari M., Thielemann F.-K., 2015, *MNRAS*, 452, 1970
- Winteler C., Käppeli R., Perego A., Arcones A., Vasset N., Nishimura N., Liebendörfer M., Thielemann F.-K., 2012,

ApJ, 750, L22
Woosley S. E., Hoffman R. D., 1992, ApJ, 395, 202
Woosley S. E., Howard W. M., 1978, ApJS, 36, 285
Wu M.-R., Fernández R., Martínez-Pinedo G., Metzger
B. D., 2016, MNRAS, 463, 2323

APPENDIX A:

The list of stellar parameters and the Mo and Ru abundances is given in Table A1; The comparison of parameters is presented in Table A2. Figs. A1, A2 and A3 illustrate the following correlations: Mo vs. Y, Zr, Sm and Sr; Sr vs. Y; Ru vs. Ba, Eu and Sm.

Table A1: Stellar parameters and abundances of Mo and Ru.

HD BD	T_{eff} , K	$\log g$	[Fe/H]	V_t , km s $^{-1}$	[Mo/Fe]	stand deviation	[Ru/Fe]	stand deviation
thin disc								
166	5514	4.6	0.16	0.6	-0.05	0.04	–	–
1562	5828	4	-0.32	1.2	0.18	0.04	0.29	0.08
1835	5790	4.5	0.13	1.1	–	–	–	–
3651	5277	4.5	0.15	0.6	-0.01	0.06	-0.08	0.08
4256	5020	4.3	0.08	1.1	–	–	–	–
4307	5889	4	-0.18	1.1	0.24	0.04	–	–
4614	5965	4.4	-0.24	1.1	< 0.21	0.06	0.16	0.06
5294	5779	4.1	-0.17	1.3	0.25	0.07	0.35	0.11
6660	4759	4.6	0.08	1.4	0.08	0.03	0.17	0.07
7590	5962	4.4	-0.1	1.4	< 0.28	0.07	0.3	–
7924	5165	4.4	-0.22	1.1	0.19	0.05	0.16	0.08
8648	5790	4.2	0.12	1.1	0.06	0.04	–	–
9407	5666	4.45	0.05	0.8	-0.01	0.08	0.02	0.06
9826	6074	4	0.1	1.3	< 0.03	0.00	–	–
10086	5696	4.3	0.13	1.2	0.02	0.04	0.02	–
10307	5881	4.3	0.02	1.1	0.01	0.03	–	–
10476	5242	4.3	-0.05	1.1	0.11	0.08	0.2	0.1
10780	5407	4.3	0.04	0.9	0.14	0.07	-0.03	0.04
11007	5980	4	-0.2	1.1	0.18	0.07	0.18	0.09
11373	4783	4.65	0.08	1	-0.05	0.00	0.04	0.07
12846	5766	4.5	-0.24	1.2	0.37	–	0.14	–
13507	5714	4.5	-0.02	1.1	0.1	0.00	0.1	0.06
14374	5449	4.3	-0.09	1.1	0.22	0.07	–	–
16160	4829	4.6	-0.16	1.1	0.17	0.04	0.26	0.15
17674	5909	4	-0.14	1.1	0.07	0.07	0.28	0.01
17925	5225	4.3	-0.04	1.1	0.22	0.07	–	–
18632	5104	4.4	0.06	1.4	0.16	0.06	–	–
18803	5665	4.55	0.14	0.8	-0.11	0.07	-0.11	0.03
19019	6063	4	-0.17	1.1	< 0.18	0.04	–	–
19373	5963	4.2	0.06	1.1	< -0.02	0.05	-0.12	0.01
20630	5709	4.5	0.08	1.1	-0.03	0.04	0.05	0.1
22049	5084	4.4	-0.15	1.1	0.18	0.07	–	–
22484	6037	4.1	-0.03	1.1	< 0.04	0.00	-0.15	0.03
22556	6155	4.2	-0.17	1.1	–	–	–	–
24053	5723	4.4	0.04	1.1	0.11	0.04	0.23	0.03
24238	4996	4.3	-0.46	1	0.27	0.04	0.41	0.07
24496	5536	4.3	-0.13	1.5	0.21	0.00	0.08	0.07
25665	4967	4.7	0.01	1.2	-0.01	0.00	–	–
25680	5843	4.5	0.05	1.1	0.05	0.04	-0.05	–
26923	5920	4.4	-0.03	1	-0.04	0.00	0.29	0.01
28005	5980	4.2	0.23	1.1	-0.08	0.11	0.00	0.08
28447	5639	4	-0.09	1.1	-0.03	0.07	-0.06	–
29150	5733	4.3	0.00	1.1	-0.01	0.11	-0.04	0.01
29310	5852	4.2	0.08	1.4	–	–	–	–
29645	6009	4	0.14	1.3	-0.04	0.04	0.11	–
30495	5820	4.4	-0.05	1.3	< 0.09	0.01	–	–
33632	6072	4.3	-0.24	1.1	< -0.03	0.07	–	–
34411	5890	4.2	0.1	1.1	-0.09	0.03	–	–
37008	5016	4.4	-0.41	0.8	0.14	0.04	0.2	0.04
37394	5296	4.5	0.09	1.1	0.08	0.13	–	–
38858	5776	4.3	-0.23	1.1	0.13	0.04	0.26	0.04
39587	5955	4.3	-0.03	1.5	-0.09	0.07	0.16	0.04
40616	5881	4	-0.22	1.1	0.13	0.04	0.12	0.07
41330	5904	4.1	-0.18	1.2	0.19	0.00	–	–
41593	5312	4.3	-0.04	1.1	0.19	0.05	0.26	0.1
42618	5787	4.5	-0.07	1	0.08	0.11	0.12	0.07
42807	5719	4.4	-0.03	1.1	0.06	0.07	0.13	0.07
43587	5927	4.1	-0.11	1.3	0.12	0.04	0.11	–

HD/BD	T_{eff} , K	$\log g$	[Fe/H]	Vt, km s ⁻¹	[Mo/Fe]	stand deviation	[Ru/Fe]	stand deviation
thin disc								
43856	6143	4.1	-0.19	1.1	–	–	–	–
43947	6001	4.3	-0.24	1.1	–	–	–	–
45088	4959	4.3	-0.21	1.2	0.09	–	–	–
47752	4613	4.6	-0.05	0.2	0.03	0.07	0.05	0.07
48682	5989	4.1	0.05	1.3	-0.02	0.06	0.05	0.00
50281	4712	3.9	-0.2	1.6	–	–	–	–
50692	5911	4.5	-0.1	0.9	0.21	0.04	0.00	–
51419	5746	4.1	-0.37	1.1	0.24	0.01	–	–
51866	4934	4.4	0.00	1	0.08	0.04	0.00	–
53927	4860	4.64	-0.22	1.2	0.01	0.05	0.14	0.12
54371	5670	4.2	0.06	1.2	0.07	0.07	0.12	–
55575	5949	4.3	-0.31	1.1	0.09	0.07	0.26	0.05
58595	5707	4.3	-0.31	1.2	0.29	0.07	0.54	0.11
59747	5126	4.4	-0.04	1.1	0.12	0.00	0.04	–
61606	4956	4.4	-0.12	1.3	0.24	0.08	–	–
62613	5541	4.4	-0.1	1.1	0.16	0.04	0.17	0.11
63433	5693	4.35	-0.06	1.9	0.21	0.04	0.11	0.07
64468	5014	4.2	0.00	1.2	0.18	0.07	0.03	0.08
64815	5864	4	-0.33	1.1	0.26	–	–	–
65874	5936	4	0.05	1.3	-0.11	0.02	–	–
66573	5821	4.6	-0.53	1.1	0.32	0.01	0.57	0.06
68638	5430	4.4	-0.24	1.1	0.25	0.02	–	–
70923	5986	4.2	0.06	1.1	-0.07	0.06	0.04	–
71148	5850	4.2	0.00	1.1	0.02	0.01	0.05	0.00
72760	5349	4.1	0.01	1.1	–	–	–	–
72905	5884	4.4	-0.07	1.5	0.13	0.04	0.12	–
73344	6060	4.1	0.08	1.1	<-0.02	0.11	0.07	–
73667	4884	4.4	-0.58	0.9	0.16	0.03	0.39	0.1
75732	5373	4.3	0.25	1.1	0.01	0.04	-0.11	0.07
75767	5823	4.2	-0.01	0.9	-0.06	0.00	–	–
76151	5776	4.4	0.05	1.1	-0.02	0.07	–	–
79969	4825	4.4	-0.05	1	–	–	–	–
82106	4827	4.1	-0.11	1.1	0.22	0.04	0.09	0.03
82443	5334	4.4	-0.03	1.3	-0.01	0.09	–	–
87883	5015	4.4	0.00	1.1	0.03	0.07	–	–
88072	5778	4.3	0.00	1.1	0.03	0.06	-0.05	–
89251	5886	4	-0.12	1.1	0.05	0.07	–	–
89269	5674	4.4	-0.23	1.1	0.06	0.07	0.21	0.06
91347	5931	4.4	-0.43	1.1	0.31	0.00	0.43	–
94765	5077	4.4	-0.01	1.1	0.14	0.07	0.08	0.04
95128	5887	4.3	0.01	1.1	-0.03	0.07	0.19	–
97334	5869	4.4	0.06	1.2	0.00	0.11	–	–
97658	5136	4.5	-0.32	1.2	0.12	0.02	0.07	0.03
98630	6060	4	0.22	1.4	–	–	–	–
101177	5932	4.1	-0.16	1.1	< 0.15	0.06	0.21	–
102870	6055	4	0.13	1.4	<-0.15	0.00	-0.13	0.00
105631	5416	4.4	0.16	1.2	–	–	–	–
107705	6040	4.2	0.06	1.4	< 0.04	0.04	–	–
108954	6037	4.4	-0.12	1.1	< 0.1	0.07	–	–
109358	5897	4.2	-0.18	1.1	0.06	0.07	0.18	0.05
110463	4950	4.5	-0.05	1.2	0.13	0.07	0.13	0.08
110833	5075	4.3	0.00	1.1	0.13	0.00	0.00	0.07
111395	5648	4.6	0.1	0.9	–	–	–	–
112758	5203	4.2	-0.56	1.1	–	–	–	–
114710	5954	4.3	0.07	1.1	-0.06	0.05	-0.04	–
115383	6012	4.3	0.11	1.1	<-0.02	0.00	–	–
115675	4745	4.45	0.02	1	–	–	–	–
116443	4976	3.9	-0.48	1.1	–	–	–	–
116956	5386	4.55	0.08	1.2	-0.03	0.04	-0.03	0.07
117043	5610	4.5	0.21	0.4	-0.11	0.02	-0.14	0.04

HD/BD	T_{eff} , K	$\log g$	[Fe/H]	Vt, km s ⁻¹	[Mo/Fe]	stand deviation	[Ru/Fe]	stand deviation
thin disc								
119802	4763	4	-0.05	1.1	0.06	0.04	-0.05	–
122064	4937	4.5	0.07	1.1	–	–	–	–
124642	4722	4.65	0.02	1.3	–	–	–	–
125184	5695	4.3	0.31	0.7	-0.18	0.00	-0.13	0.04
126053	5728	4.2	-0.32	1.1	< 0.1	0.00	0.35	0.04
127506	4542	4.6	-0.08	1.2	–	–	–	–
128311	4960	4.4	0.03	1.3	0.1	0.07	0.02	0.07
130307	4990	4.3	-0.25	1.4	0.28	0.07	0.23	0.04
130948	5943	4.4	-0.05	1.3	< 0.06	0.04	–	–
131977	4683	3.7	-0.24	1.8	–	–	–	–
135599	5257	4.3	-0.12	1	0.2	0.00	0.22	0.00
137107	6037	4.3	0.00	1.1	–	–	–	–
139777	5771	4.4	0.01	1.3	–	–	–	–
139813	5408	4.5	0.00	1.2	0.08	0.00	–	–
140538	5675	4.5	0.02	0.9	0.03	0.06	0.13	–
141004	5884	4.1	-0.02	1.1	<-0.03	0.04	-0.13	–
141272	5311	4.4	-0.06	1.3	0.09	0.07	0.06	0.07
142267	5856	4.5	-0.37	1.1	0.25	0.07	0.55	0.04
144287	5414	4.5	-0.15	1.1	0.16	0.04	0.18	0.04
145675	5406	4.5	0.32	1.1	–	–	–	–
146233	5799	4.4	0.01	1.1	–	–	–	–
149661	5294	4.5	-0.04	1.1	0.07	0.07	0.01	0.04
149806	5352	4.55	0.25	0.4	–	–	–	–
151541	5368	4.2	-0.22	1.3	–	–	–	–
153525	4810	4.7	-0.04	1	–	–	–	–
154345	5503	4.3	-0.21	1.3	0.14	0.00	0.19	0.08
156668	4850	4.2	-0.07	1.2	0.13	0.06	0.19	0.06
156985	4790	4.6	-0.18	1	0.14	0.04	0.18	0.07
158633	5290	4.2	-0.49	1.3	0.25	0.04	0.31	0.04
160346	4983	4.3	-0.1	1.1	0.18	0.07	0.15	–
161098	5617	4.3	-0.27	1.1	0.17	0.04	–	–
164922	5392	4.3	0.04	1.1	–	–	–	–
165173	5505	4.3	-0.05	1.1	0.04	0.09	–	–
165341	5314	4.3	-0.08	1.1	0.16	0.07	0.13	–
165476	5845	4.1	-0.06	1.1	–	–	–	–
165670	6178	4	-0.1	1.5	–	–	–	–
165908	5925	4.1	-0.6	1.1	< 0.28	0.07	0.45	–
166620	5035	4	-0.22	1	0.12	0.04	0.17	–
171314	4608	4.65	0.07	1	–	–	–	–
174080	4764	4.55	0.04	1	0.01	0.04	-0.04	–
175742	5030	4.5	-0.03	2	–	–	–	–
176377	5901	4.4	-0.17	1.3	< 0.2	0.00	0.22	–
176841	5841	4.3	0.23	1.1	< -0.1	0.07	-0.08	–
178428	5695	4.4	0.14	1	-0.11	0.00	0.01	–
180161	5473	4.5	0.18	1.1	0.02	0.09	-0.13	–
182488	5435	4.4	0.07	1.1	0.06	0.07	-0.07	–
183341	5911	4.3	-0.01	1.3	–	–	–	–
184385	5536	4.45	0.12	0.9	-0.07	0.04	-0.12	0.05
185144	5271	4.2	-0.33	1.1	0.16	0.00	0.1	0.04
185414	5818	4.3	-0.04	1.1	–	–	–	–
186408	5803	4.2	0.09	1.1	-0.01	0.07	0.06	–
186427	5752	4.2	0.02	1.1	-0.01	0.01	–	–
187897	5887	4.3	0.08	1.1	0.00	0.07	0.02	0.00
189087	5341	4.4	-0.12	1.1	–	–	–	–
189733	5076	4.4	-0.03	1.5	-0.01	0.07	0.16	0.04
190007	4724	4.5	0.16	0.8	0.1	0.04	-0.11	–
190406	5905	4.3	0.05	1	-0.02	0.03	–	–
190470	5130	4.3	0.11	1	0.02	0.07	-0.03	0.03
190771	5766	4.3	0.13	1.5	0.05	0.07	–	–
191533	6167	3.8	-0.1	1.5	–	–	–	–

HD/BD	T_{eff} , K	$\log g$	[Fe/H]	Vt, km s ⁻¹	[Mo/Fe]	stand deviation	[Ru/Fe]	stand deviation
thin disc								
191785	5205	4.2	-0.12	1.2	0.14	0.08	0.15	0.04
195005	6075	4.2	-0.06	1.3	–	–	–	–
195104	6103	4.3	-0.19	1.1	–	–	–	–
197076	5821	4.3	-0.17	1.2	0.2	–	0.12	–
199960	5878	4.2	0.23	1.1	-0.13	0.04	-0.18	–
200560	5039	4.4	0.06	1.1	0.12	0.00	0.04	–
202108	5712	4.2	-0.21	1.1	0.17	0.04	0.16	–
202575	4667	4.6	-0.03	0.5	-0.01	0.05	0.00	0.04
203235	6071	4.1	0.05	1.3	–	–	–	–
205702	6020	4.2	0.01	1.1	–	–	–	–
206860	5927	4.6	-0.07	1.8	–	–	–	–
208038	4982	4.4	-0.08	1	–	–	–	–
208313	5055	4.3	-0.05	1	0.06	0.04	0.1	0.03
208906	5965	4.2	-0.8	1.7	–	–	–	–
210667	5461	4.5	0.15	0.9	0.08	0.07	-0.08	0.04
210752	6014	4.6	-0.53	1.1	< 0.26	0.00	–	–
211472	5319	4.4	-0.04	1.1	0.15	0.04	0.04	0.05
214683	4747	4.6	-0.46	1.2	0.11	0.04	0.28	0.05
216259	4833	4.6	-0.55	0.5	–	–	–	–
216520	5119	4.4	-0.17	1.4	–	–	–	–
217014	5763	4.3	0.17	1.1	-0.06	0.11	-0.05	0.06
217813	5845	4.3	0.03	1.5	0.1	–	0.02	–
218868	5547	4.45	0.21	0.4	–	–	–	–
219538	5078	4.5	-0.04	1.1	–	–	–	–
219623	5949	4.2	0.04	1.2	0.09	–	-0.04	–
220140	5144	4.6	-0.03	2.4	–	–	–	–
220182	5364	4.5	-0.03	1.2	0.08	0.04	0.13	–
220221	4868	4.5	0.16	0.5	0.05	0.04	-0.04	0.06
221851	5184	4.4	-0.09	1	–	–	–	–
222143	5823	4.45	0.15	1.1	-0.04	0.05	-0.05	0.07
224465	5745	4.5	0.08	0.8	-0.07	0.04	-0.08	–
263175	4734	4.5	-0.16	0.5	0.08	0.06	0.19	0.04
BD12063	4859	4.4	-0.22	0.6	-0.07	0.04	0.04	0.04
BD124499	4678	4.7	0.00	0.5	–	–	–	–
thick disc								
245	5400	3.4	-0.84	0.7	0.3	0.04	–	–
3765	5079	4.3	0.01	1.1	0.09	0.02	0.07	0.08
5351	4378	4.6	-0.21	0.5	–	–	–	–
6582	5350	4.5	-0.83	0.4	0.37	0.01	0.4	0.03
13783	5350	4.1	-0.75	1.1	0.33	–	0.32	0.04
18757	5741	4.3	-0.25	1	0.21	0.04	0.22	0.05
22879	5825	4.42	-0.91	0.9	< 0.4	0.00	0.63	0.04
65583	5373	4.6	-0.67	0.7	0.38	0.04	0.44	0.04
76932	5840	4	-0.95	1	< 0.33	0.07	–	–
106516	6165	4.4	-0.72	1.1	0.35	–	–	–
110897	5925	4.2	-0.45	1.1	0.21	0.04	0.34	0.07
135204	5413	4	-0.16	1.1	0.19	0.00	0.1	0.07
152391	5495	4.3	-0.08	1.3	0.16	0.07	0.03	0.07
157089	5785	4	-0.56	1	0.27	0.04	–	–
157214	5820	4.5	-0.29	1	0.27	0.1	0.53	0.07
159062	5414	4.3	-0.4	1	0.38	0.03	0.42	0.08
165401	5877	4.3	-0.36	1.1	0.27	0.04	0.55	–
190360	5606	4.4	0.12	1.1	0.06	0.14	-0.03	–
201889	5600	4.1	-0.85	1.2	0.63	0.07	0.52	–
201891	5850	4.4	-0.96	1	0.47	0.04	0.65	–
204521	5809	4.6	-0.66	1.1	0.47	0.11	0.45	–
Hercules stream								
13403	5724	4	-0.31	1.1	0.19	0.03	0.21	0.07
19308	5844	4.3	0.08	1.1	-0.08	0.11	-0.03	0.05
23050	5929	4.4	-0.36	1.1	0.34	0.07	0.31	–

HD/BD	T_{eff} , K	$\log g$	[Fe/H]	Vt, km s ⁻¹	[Mo/Fe]	stand deviation	[Ru/Fe]	stand deviation
thin disc								
30562	5859	4	0.18	1.1	–	–	–	–
64606	5250	4.2	-0.91	0.8	0.40	0.02	0.66	0.07
68017	5651	4.2	-0.42	1.1	0.25	0.00	0.32	–
81809	5782	4	-0.28	1.3	< 0.31	0.07	0.28	–
107213	6156	4.1	0.07	1.6	<0.01	0.00	–	–
139323	5204	4.6	0.19	0.7	–	–	–	–
139341	5242	4.6	0.21	0.9	–	–	–	–
144579	5294	4.1	-0.7	1.3	0.40	0.04	0.45	0.07
159222	5834	4.3	0.06	1.2	0.07	0.07	0.01	0.04
159909	5749	4.1	0.06	1.1	-0.08	0.07	–	–
215704	5418	4.2	0.07	1.1	–	–	–	–
218209	5705	4.5	-0.43	1	0.31	–	0.38	–
221354	5242	4.1	-0.06	1.2	0.13	0.08	-0.01	–
nonclassified								
4628	4905	4.6	-0.36	0.5	0.21	0.04	0.21	–
4635	5103	4.4	0.07	0.8	0.08	0.04	0.13	0.07
10145	5673	4.4	-0.01	1.1	–	–	–	–
12051	5458	4.55	0.24	0.5	-0.12	0.07	-0.24	–
13974	5590	3.8	-0.49	1.1	–	–	–	–
17660	4713	4.75	0.17	1.3	–	–	–	–
20165	5145	4.4	-0.08	1.1	0.20	0.07	0.13	0.07
24206	5633	4.5	-0.08	1.1	0.15	0.07	0.06	0.04
32147	4945	4.4	0.13	1.1	–	–	–	–
45067	6058	4	-0.02	1.2	–	–	–	–
84035	4808	4.8	0.25	0.5	–	–	–	–
86728	5725	4.3	0.22	0.9	–	–	–	–
90875	4788	4.5	0.24	0.5	–	–	–	–
117176	5611	4	-0.03	1	0.05	0.03	-0.01	0.00
117635	5230	4.3	-0.46	0.7	0.33	0.07	–	–
154931	5910	4	-0.1	1.1	–	–	–	–
159482	5620	4.1	-0.89	1	–	–	–	–
168009	5826	4.1	-0.01	1.1	0.11	0.07	-0.03	–
173701	5423	4.4	0.18	1.1	0.04	0.07	-0.03	–
182736	5430	3.7	-0.06	1	–	–	–	–
184499	5750	4	-0.64	1.5	<0.34	0.04	0.69	–
184768	5713	4.2	-0.07	1.1	–	–	–	–
186104	5753	4.2	0.05	1.1	–	–	–	–
215065	5726	4	-0.43	1.1	0.30	0.07	0.38	0.07
219134	4900	4.2	0.05	0.8	0.12	0.00	–	–
219396	5733	4	-0.1	1.2	0.10	0.04	0.20	–
224930	5300	4.1	-0.91	0.7	0.26	0.04	0.26	–

Table A2. Parameters of our target stars and their comparison with with those reported in Adibekyan et al. (2014); Nissen & Schuster (2011); Feltzing, Fohlman & Bensby (2007); Takeda (2007) for common stars.

HD	T_{eff} , K	$\log g$	[Fe/H]	HD	T_{eff} , K	$\log g$	[Fe/H]	ΔT_{eff} , K	$\Delta \log g$	Δ [Fe/H]
our				Adibekyan et al. (2014)						
4307	5889	4	-0.18	4307	5812	4.1	-0.23	77	-0.1	0.05
14374	5449	4.3	-0.09	14374	5425	4.48	-0.04	24	-0.18	-0.05
22879	5972	4.5	-0.77	22879	5884	4.52	-0.82	88	-0.02	0.05
38858	5776	4.3	-0.23	38858	5733	4.51	-0.22	43	-0.21	-0.01
125184	5695	4.3	0.31	125184	5680	4.1	0.27	15	0.2	0.04
146233	5799	4.4	0.01	146233	5818	4.45	0.04	-19	-0.05	-0.03
161098	5617	4.3	-0.27	161098	5560	4.46	-0.27	57	-0.16	0
199960	5878	4.2	0.23	199960	5973	4.39	0.28	-95	-0.19	-0.05
210752	6014	4.6	-0.53	210752	5951	4.53	-0.58	63	0.07	0.05
our				Nissen & Schuster (2011)						
22879	5972	4.5	-0.77	22879	5759	4.25	-0.85	213	0.25	0.08
76932	5840	4	-0.95	76932	5877	4.13	-0.87	-37	-0.13	-0.08
106516	6165	4.4	-0.72	106516	6196	4.42	-0.68	-31	-0.02	-0.04
159482	5620	4.1	-0.89	159482	5737	4.31	-0.73	-117	-0.21	-0.16
our				Feltzing, Fohlman & Bensby (2007)						
22879	5972	4.5	-0.77	22879	5920	4.33	-0.84	52	0.17	0.07
30495	5820	4.4	-0.05	30495	5850	4.5	0.05	-30	-0.1	-0.1
76932	5840	4	-0.95	76932	5875	4.1	-0.91	-35	-0.1	-0.04
152391	5495	4.3	-0.08	152391	5470	4.55	-0.02	25	-0.25	-0.06
157089	5785	4	-0.56	157089	5830	4.06	-0.57	-45	-0.06	0.01
165401	5877	4.3	-0.36	165401	5720	4.35	-0.46	157	-0.05	0.1
176377	5901	4.4	-0.17	176377	5810	4.4	-0.28	91	0	0.11
190360	5606	4.4	0.12	190360	5490	4.23	0.25	116	0.17	-0.13
199960	5878	4.2	0.23	199960	5940	4.26	0.27	-62	-0.06	-0.04
217014	5763	4.3	0.17	217014	5789	4.34	0.2	-26	-0.04	-0.03
our				Takeda (2007)						
4307	5889	4	-0.18	4307	5648.1	3.747	-0.289	240.9	0.253	0.109
4614	5965	4.4	-0.24	4614	5915.4	4.462	-0.214	49.6	-0.062	-0.026
4628	4905	4.6	-0.36	4628	5009.3	4.62	-0.243	-104.3	-0.02	-0.117
6582	5240	4.3	-0.94	6582	5330.7	4.539	-0.811	-90.7	-0.239	-0.129
10307	5881	4.3	0.02	10307	5890.9	4.36	0.058	-9.9	-0.06	-0.038
10476	5242	4.3	-0.05	10476	5196.3	4.504	-0.011	45.7	-0.204	-0.039
10780	5407	4.3	0.04	10780	5427.1	4.632	0.1	-20.1	-0.332	-0.06
17925	5225	4.3	-0.04	17925	5235.2	4.669	0.133	-10.2	-0.369	-0.173
18803	5665	4.55	0.14	18803	5665.7	4.455	0.146	-0.7	0.095	-0.006
20630	5709	4.5	0.08	20630	5768.6	4.544	0.107	-59.6	-0.044	-0.027
30562	5859	4	0.18	30562	5908.3	4.084	0.232	-49.3	-0.084	-0.052
34411	5890	4.2	0.1	34411	5888.6	4.232	0.107	1.4	-0.032	-0.007
81809	5782	4	-0.28	81809	5619.6	4.018	-0.345	162.4	-0.018	0.065
86728	5725	4.3	0.22	86728	5837.9	4.421	0.268	-112.9	-0.121	-0.048
110897	5925	4.2	-0.45	110897	5841.6	4.325	-0.503	83.4	-0.125	0.053
111395	5648	4.6	0.1	111395	5631.7	4.485	0.105	16.3	0.115	-0.005
115383	6012	4.3	0.11	115383	6119.7	4.251	0.214	-107.7	0.049	-0.104
117176	5611	4	-0.03	117176	5466.4	3.799	-0.112	144.6	0.201	0.082
125184	5695	4.3	0.31	125184	5629.6	4.015	0.247	65.4	0.285	0.063
141004	5884	4.1	-0.02	141004	5877	4.113	-0.008	7	-0.013	-0.012
149661	5294	4.5	-0.04	149661	5288.6	4.607	0.053	5.4	-0.107	-0.093
157214	5820	4.5	-0.29	157214	5693.2	4.214	-0.369	126.8	0.286	0.079
165908	5925	4.1	-0.6	165908	6183.1	4.347	-0.456	-258.1	-0.247	-0.144
178428	5695	4.4	0.14	178428	5660.3	4.189	0.162	34.7	0.211	-0.022
182488	5435	4.4	0.07	182488	5417.1	4.578	0.214	17.9	-0.178	-0.144
190406	5905	4.3	0.05	190406	5944.3	4.396	0.056	-39.3	-0.096	-0.006
197076	5821	4.3	-0.17	197076	5804.7	4.405	-0.075	16.3	-0.105	-0.095
199960	5878	4.2	0.23	199960	5924	4.26	0.275	-46	-0.06	-0.045
217014	5763	4.3	0.17	217014	5779.1	4.298	0.203	-16.1	0.002	-0.033
219623	5949	4.2	0.04	219623	6103	4.185	0.049	-154	0.015	-0.009
224930	5300	4.1	-0.91	224930	5680.5	4.863	-0.522	-380.5	-0.763	-0.388

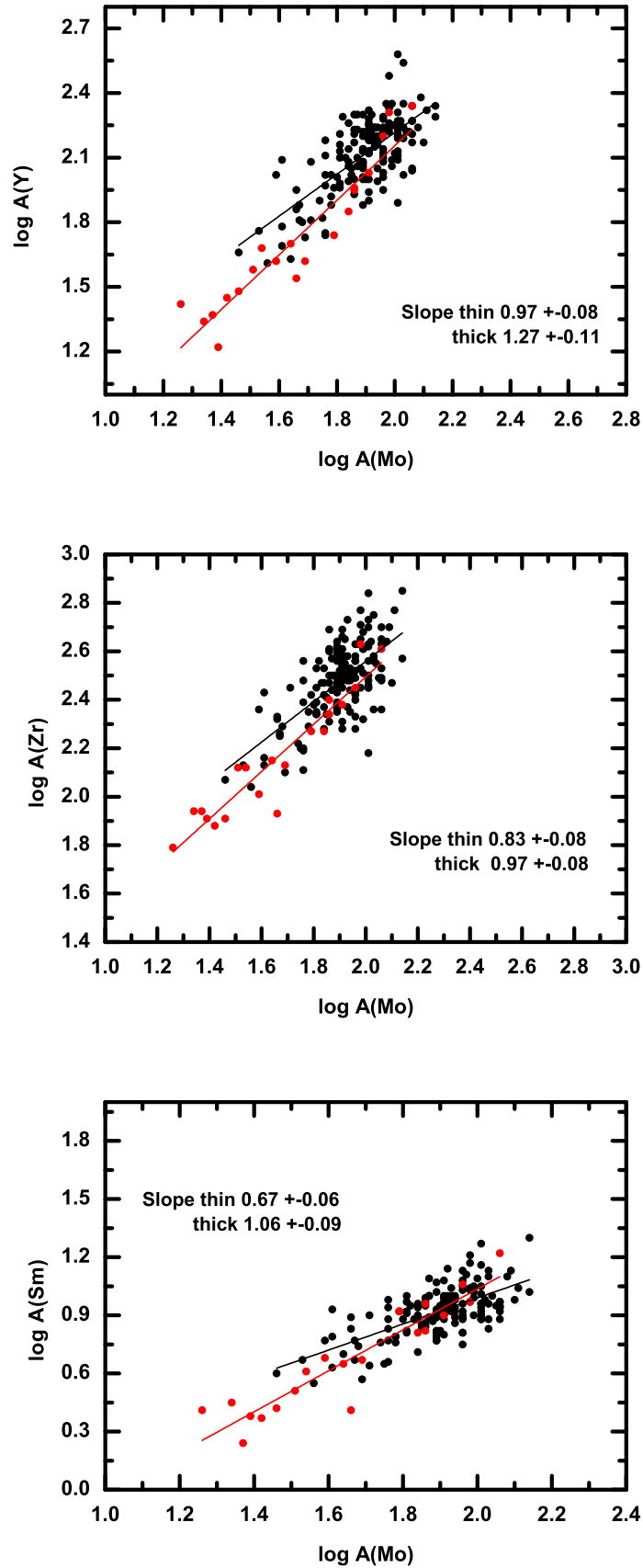


Figure A1. Trends for $\log A(\text{El})$ where $\text{El} = \text{Y}, \text{Zr}, \text{Sm}$ with respect to $\log A(\text{Mo})$. Notation is the same as presented in Fig. 6.

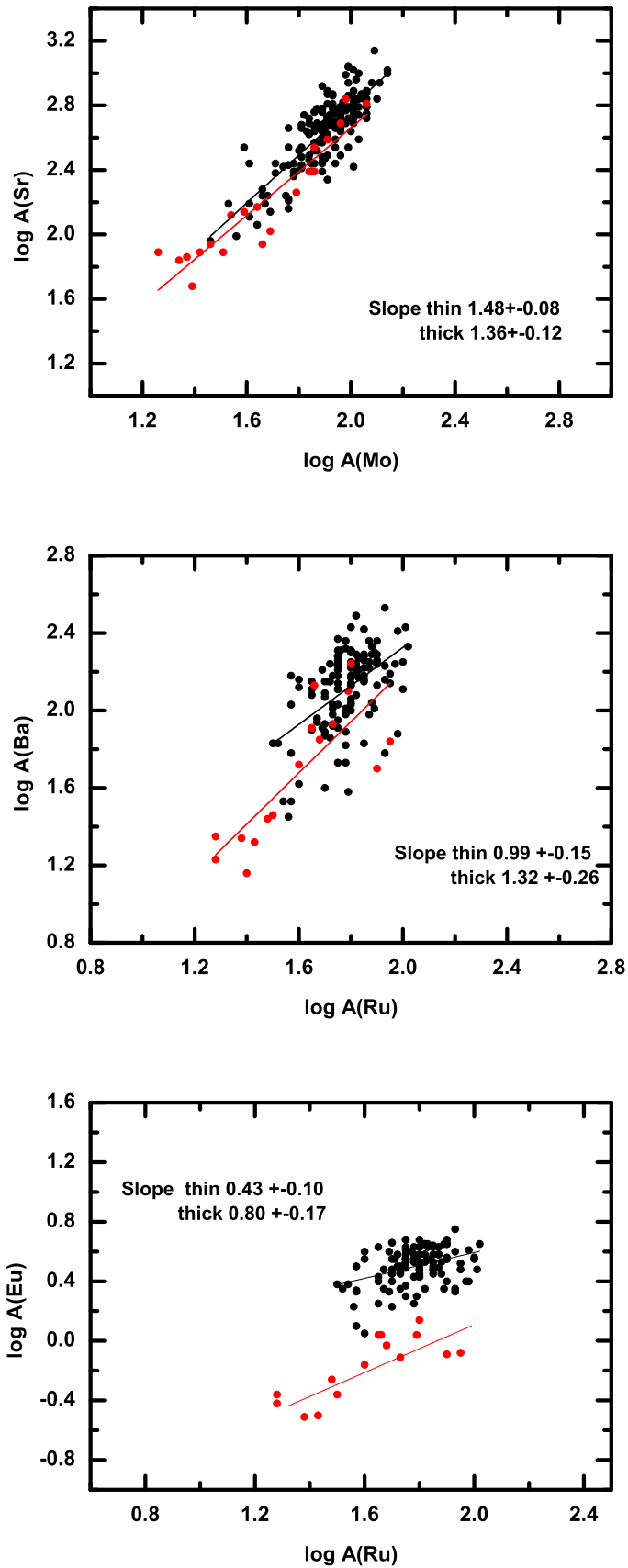


Figure A2. Trends of log A(Sr) vs. log A(Mo) and log A(Eu) where El = Ba, and Eu vs. log A(Ru). Notation is the same as presented in Fig. 6.

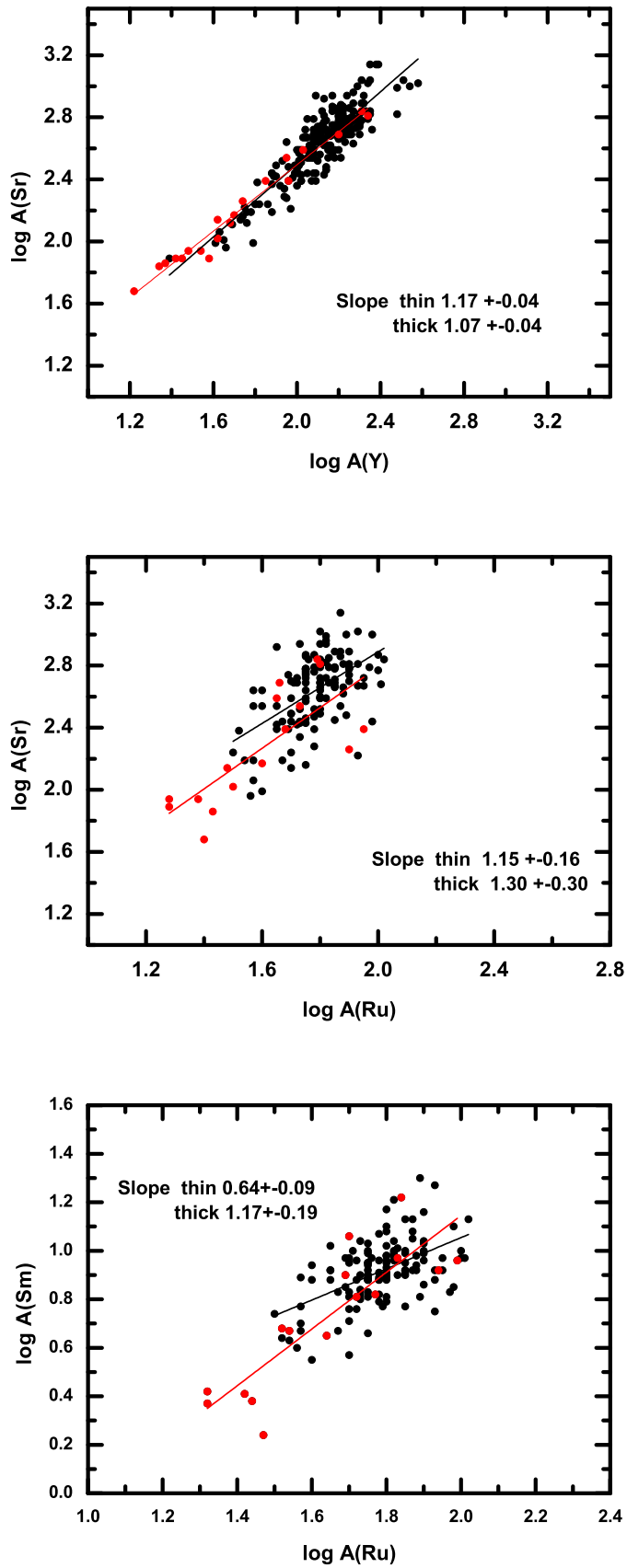


Figure A3. Trends for logA(Sr) vs. logA(Y) and log A(El) where El = Sr and Sm vs. log A(Ru). Notation is the same as presented in